Reconstruction of Indian summer monsoon winds and precipitation over the past 10,000 years using equatorial pacific SST proxy records

Emily C. Gill[1,2] (iD), **Balaji Rajagopalan[1,2]** (iD), **Peter H. Molnar[2,3]** (iD), **Yochanan Kushnir[4]** (iD), **and Thomas M. Marchitto[3,5]** (iD)

[1]Department of Civil, Environmental and Architectural Engineering, University of Colorado Boulder, Boulder, Colorado, USA, [2]Cooperative Institute for Research in Environmental Sciences, Boulder, Colorado, USA, [3]Department of Geological Sciences, University of Colorado Boulder, Boulder, Colorado, USA, [4]Lamont-Doherty Earth Observatory, Columbia University, Palisades, New York, USA, [5]Institute of Arctic and Alpine Research, University of Colorado Boulder, Boulder, Colorado, USA

Abstract Using a multiproxy reduced dimension methodology, we reconstruct fields of Arabian Sea summer wind stress curl and Indian monsoon rainfall anomalies since early Holocene using sea surface temperature (SST) proxies (Mg/Ca and alkenones) from 27 locations scattered across the equatorial Pacific. Reconstructions of summer wind stress curl reveal positive anomalies of ~30% greater than present day off the coastlines of Oman and Yemen at 10 ka, suggesting enhanced ocean upwelling and an enhanced monsoon jet during this time. Positive wind stress curl anomalies in these regions continued but weakened to ~12% greater than present day at 6 ka. Wind stress curl anomalies increased by about 8% from 6 to 4 ka but declined again until 2 ka. Positive anomalies in wind stress curl during the early to middle Holocene are consistent with greater early Holocene abundances of the upwelling indicator *Globigerina bulloides* in the western Arabian Sea, which accumulates most rapidly in present climates during periods of marked upwelling. Spatial rainfall reconstructions reveal the greatest difference in precipitation at 10 ka over the core monsoon region (~20–60% greater than present day) and concurrently the greatest deficit in rainfall in North East India and on the eastern side of the Western Ghats (~10–30% less than present day). Specifically, reconstructions for 10 ka reveal 40–60% greater rainfall than present day over northwest India. These findings advance the hypothesis that teleconnections from the equatorial Pacific contributed to, if not accounted for, greater early to middle Holocene wetness over India as recorded by various (e.g., cave, lacustrine, and discharge) paleoclimate proxies throughout the monsoon region.

1. Introduction

Paleoclimatic evidence from proxy data suggests that India has aridified over the past 10,000 years (ka) (Figure 1). The predominantly cited explanation rests on the idea that greater summer insolation in early Holocene time, due to the precessional cycle, caused greater heating of the Indian subcontinent, which increased the land-ocean temperature gradient and created a stronger early than late Holocene monsoon [e.g., *Kutzbach*, 1981; *Kutzbach and Otto-Bliesner*, 1982; *Liu et al.*, 2000, 2003, 2004]. This idea relies on the traditional understanding of monsoon dynamics. The monsoon begins each year in mid-May due to the intense spring heating of the Indian subcontinent and possibly the Tibetan Plateau, which creates a temperature, and thus, surface pressure gradient, between the land and the surrounding ocean that forces the monsoon jet [e.g., *Li and Yanai*, 1996; *Wu et al.*, 2007], at least during the early (mid-May to mid-June) and late (September to mid-October) seasons [*Rajagopalan and Molnar*, 2013]. In principle, over the course of the entire monsoon season, the degree of the local land warming can modulate the strength not only of the monsoon jet but also of rainfall. Therefore, a sensible hypothesis follows that enhanced land warming during the early to mid-Holocene contributed to greater wetness over India.

Since the mid-1990s, however, surface temperatures over India have risen dramatically while monsoon rainfall has remained below average [see *Krishna Kumar et al.*, 2011] (Figure 2). This apparent inconsistency serves as a reminder that other processes, besides summer insolation and surface heating, also affect monsoon strength, whether measured by rainfall or wind speeds.
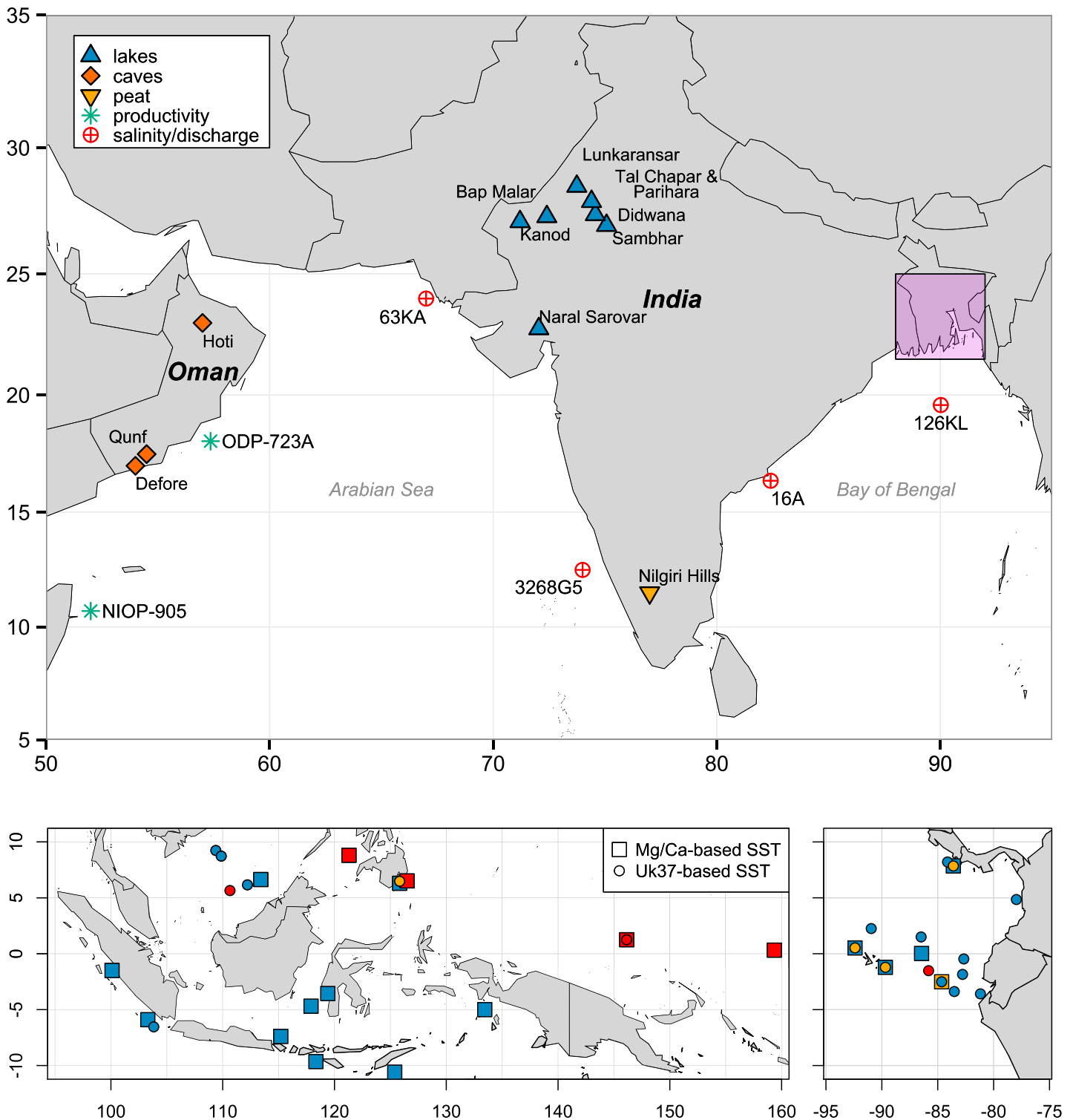
Figure 1. (top) A partial summary of the locations of different types of proxy records that have been reconstructed for the past 10 ka and suggest enhanced wetness over India during the early to mid-Holocene and aridification during the late Holocene. Types of proxy records include lakes (blue triangles), caves (orange diamonds), marine salinity and/or discharge (red circles), marine biological productivity (green stars), and peat (yellow downward triangle). This figure and the original studies citing each proxy are discussed in further detail in the section 2: Paleoclimatic Evidence of a Wetter India. (bottom) The locations of tropical Pacific Mg/Ca (squares) and $U^{k'}_{37}$ (circles) records that were considered for use in the reconstructions. Yellow and red records were discarded because they either snapped to the same grid cell as a higher-resolution record (yellow) or did not span a long enough time period (red). Blue records were ultimately used in the reconstruction.
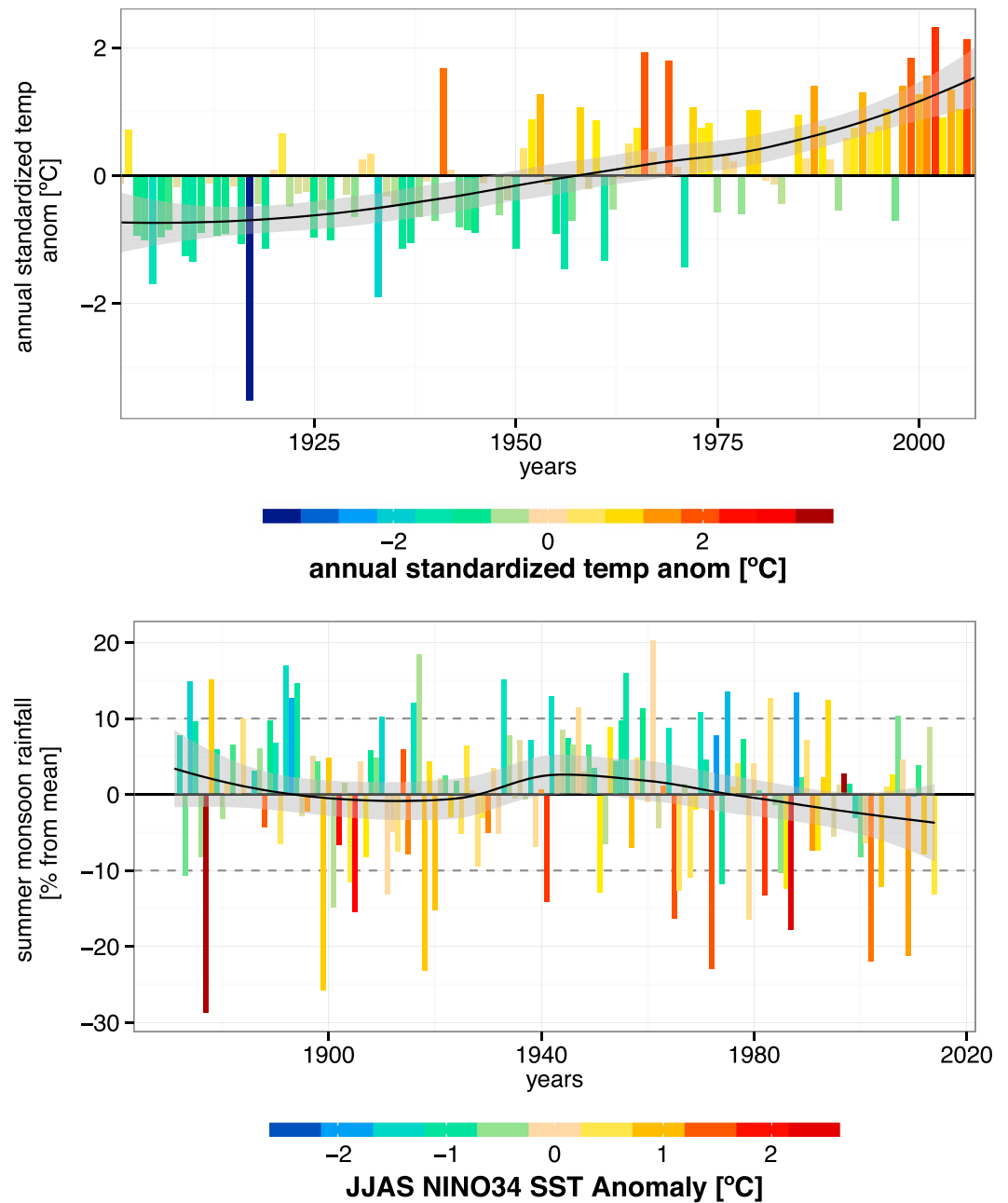
Figure 2. (top) The trend in average annual India surface temperature from 1901 to 2007 calculated using the Homogeneous India Monthly Surface temperature data set from the India Institute of Tropical Meteorology (IITM). Both bar height and color are based on the annual standardized temperature anomaly (° C). (bottom) Bar height in the bottom subpanel follows the time series of Indian summer (JJAS) monsoon rainfall represented as a percentage deviation from the mean. The color shading on the bottom panel bar plot, however, follows tropical Pacific SST anomalies (° C) from the NIÑO3.4 index region [*Kaplan et al.*, 1998] indicating whether each year was classified as La Niña (cold colors), El Niño (warm colors), or normal (neutral colors).

Teleconnections from the equatorial Pacific phenomenom—El Niño–Southern Oscillation (ENSO)—also modulate the strength of the monsoon on interannual time scales. During La Niña (El Niño), when central and eastern tropical Pacific sea surface temperatures (SSTs) are anomalously cool (warm), monsoon rainfall commonly is strong (weak). There is an asymmetry in this relationship [*Krishna Kumar et al.*, 2006] in that La Niña conditions almost always are associated with high monsoon rainfall, but El Niño conditions have historically

resulted in either normal or weak rainfall. *Krishna Kumar et al.* [2006] attribute this asymmetry to the location of El Niño-related warming in the Pacific and suggest that central Pacific warming favors drought more than eastern Pacific warming.

Proxy records from the east and west Pacific used to reconstruct SSTs throughout the past 10 ka suggest a change in the zonal SST difference along the equator akin to a shift from a more La Niña-like state during the early to mid-Holocene to a more El Niño-like state during the late Holocene [e.g., *Conroy et al.*, 2008; *Gill et al.*, 2016; *Koutavas et al.*, 2002, 2006; *Leduc et al.*, 2007, 2010; *Pahnke et al.*, 2007; *Stott et al.*, 2002, 2004]. Additionally, primary productivity records from the Banda Sea [*Beaufort et al.*, 2010] and sediment records from lakes in Ecuador and Peru [e.g., *Chazen et al.*, 2009; *Moy et al.*, 2002; *Riedinger et al.*, 2002; *Rein et al.*, 2005; *Rodbell et al.*, 1999; *Sandweiss et al.*, 1996, 2001] suggest that ENSO variability increased after the mid-Holocene. Climate model simulations that include changing insolation on orbital timescales over Holocene time also suggest a cooler equatorial Pacific and less frequent El Niño events until around 6 ka [e.g., *Clement et al.*, 1999, 2000; *Emile-Geay et al.*, 2007].

Assuming the contemporary relationship between ENSO and the monsoon persisted through the past 10 ka, and given the consistent correlation of La Niña with strong monsoon rainfall, we advance a second hypothesis that is independent of land warming over India: equatorial Pacific cooling (i.e., La Niña-like state) during the early to mid-Holocene contributed to greater rainfall over India. Following similar logic, warming in the central equatorial Pacific and the return of ENSO variability could have contributed to aridification during the late Holocene. As these two hypotheses (land warming and ENSO) are not mutually exclusive, we aim not to disprove the land-warming hypothesis but to test the plausibility of the ENSO/equatorial Pacific zonal gradient hypothesis.

Toward this end, we exploit SST proxy data from the eastern and western equatorial Pacific (Table A1). *Gill et al.* [2016] used a reduced-dimension multiproxy reconstruction approach to combine magnesium/calcium (Mg/Ca) and alkenone ($U^{k'}_{37}$) SST records from the east and west Pacific to reconstruct full fields of tropical Pacific SSTs and zonal winds. We found that the coldest eastern equatorial Pacific SST anomalies and the largest zonal difference between east and west Pacific occurred during the early Holocene (10 ka). The smallest zonal differences were seen from 4 to 2 ka. This timeline is consistent with an enhanced La Niña-like state during the early to mid-Holocene but not during the late Holocene. For the monsoonal region during early/mid-Holocene, wind stress curl and rainfall fields are of interest since various proxies have suggested increased upwelling in parts of the Arabian Sea [e.g., *Gupta et al.*, 2003] and a wetter Indian subcontinent [e.g., *Bryson and Swain*, 1981; *Swain et al.*, 1983]. These and other proxies are discussed in further detail in section 2.

Motivated by the correlation of rainfall over India with La Niña and the scattered proxy records across the Indian monsoon region in Figure 1, we ask: Could the aridification of India since 10 ka be attributed, at least in part, to teleconnections from the Pacific? We use the same reduced-dimension multiproxy reconstruction approach as *Gill et al.* [2016] to reconstruct full fields of summer wind stress curl over the Arabian Sea and Indian summer monsoon rainfall anomalies for the past 10 ka using only SST proxy records from the equatorial Pacific along with contemporary patterns of variability. From proxy SST records, it is clear that the Pacific was in a cooler state. We emphasize, however, that we do not test how or why the tropical Pacific cooled but instead test how much extra rain India *could have* received via teleconnections from a cooler tropical Pacific. We choose to reconstruct wind stress curl as it is directly related to upwelling strength, which *Gupta et al.* [2003] have shown was greater during early/mid-Holocene.

2. Paleoclimatic Evidence of a Wetter India in Early to Mid-Holocene Time

Evidence suggesting a stronger early to mid-Holocene (~10–6 ka B.P.) Indian summer monsoon includes both continental and marine proxy records from the monsoonal region of southern Oman across India to the Bay of Bengal (Figure 1). Greater precipitation during the early to mid-Holocene than late Holocene (post 4 ka) has been inferred [*Bryson and Swain*, 1981; *Swain et al.*, 1983] from pollen reconstructions [*Singh et al.*, 1972, 1973, 1974, 1990] and lake bed sediment records [*Achyuthan et al.*, 2007; *Deotare et al.*, 2004; *Enzel et al.*, 1999; *Kajale and Deotare*, 1997; *Prasad et al.*, 1997; *Wasson et al.*, 1984] from northwestern India. Although the lakes Bap Malar, Didwana, Kanod, Lunkaransar, Nal Sarovar, Sambhar, Tal Chapar, and Parihara (Figure 1, blue triangles) did not dry up simultaneously, each shows maximum wetness occurring sometime during the early to mid-Holocene, followed by a period of aridification during the late Holocene. Interestingly, a carbon isotope record obtained from peat located in Nilgiri Hills region of south India (Figure 1, yellow triangle) shows an

arid phase during the mid-Holocene followed by a wetter phase in the recent period [*Sukumar et al.*, 1993]. Though opposite to those cited above for the region to the north, this finding is actually consistent with the lake records, as this region, positioned in the rain shadow of the Western Ghats, is typically out of phase with the rest of the subcontinent in present-day rainfall [e.g., *Gill et al.*, 2015a].

Marine isotope records from sediment cores located just south of the mouths of major Indian river systems that empty into the Arabian Sea and Bay of Bengal have also been exploited to reconstruct discharge during the past 10 ka. In the Arabian Sea, *Staubwasser et al.* [2003] used $\delta^{18}O$ from the mouth of the Indus River (Figure 1, red 63KA) from the last 6 ka to infer a drastic reduction in discharge at 4.2 ka, which is concurrent with the termination of the ancient Harappan civilization that inhabited the Indus Valley. Farther south, numerous rivers drain from the Western Ghats into the eastern Arabian Sea. Oxygen isotopes from a sediment core just off the coast (Figure 1, red 3268G5) has been used to reconstruct Holocene evaporation minus precipitation, and *Sarkar et al.* [2000] inferred relatively high precipitation from 10 to 6 ka, followed by an arid episode from 3.5 to 2 ka. For the Bay of Bengal, *Ponton et al.* [2012] used a core (NGHP-16A) located at about 16°N (Figure 1, red 16A) to reconstruct changes in vegetation in the Godavari River Basin as well as salinity changes in the Bay. They report a period of aridity beginning at 4 ka and unprecedented high salinity from 3 ka to present day, implying lower precipitation and lower river discharge during the late Holocene compared to either the early or mid-Holocene. Farther north, *Kudrass et al.* [2001] used alkenone temperature data [*Sonzogni et al.*, 1998] and $\delta^{18}O$ data [*Rostek et al.*, 1993] from SO93 to 126KL (Figure 1, red 126KL) to reconstruct salinity at the mouth of the Ganges River in the northern Bay of Bengal. They found that salinity decreased during the early Holocene, reaching a minimum at 6 ka, and subsequently increased until present day. Greater salinity during late Holocene as compared to early Holocene is also supported by a record of $\delta^{18}O$ from a core in the Andaman Sea (RC12-344; not shown in Figure 1) [*Rashid et al.*, 2007]. In the same region, *Goodbred and Kuehl* [2000] analyzed over 50 sediment cores scattered across the coastal region of Bangladesh (Figure 1, purple box) to reconstruct sediment discharge from the Ganges and found high sediment discharge from 11 to 7 ka. This, combined with the findings of *Kudrass et al.* [2001], suggests that river discharge from the Ganges, which is reflective of precipitation over the Indo-Gangetic Plains, was high during the early and mid-Holocene.

Monsoon variability and strength has also been reconstructed using continental and marine records from Oman and the western Arabian Sea, where biological productivity and isotope proxies are used to infer ocean upwelling, wind strength, and precipitation for the past 10 ka. When the monsoon jet sweeps across the coast-lines of Somalia and Oman, it induces upwelling, which enhances biological productivity. *Globigerina bulloides* is a planktic foraminifer that thrives in this cold nutrient-rich upwelling water during the monsoon and acts as a proxy for wind strength [e.g., *Curry et al.*, 1992; *Prell and Curry*, 1981]. A high-resolution productivity record derived from a core off the coast of Oman (Figure 1, green star ODP-723A) reveals a monotonic decrease in *G. bulloides* between 10 and 2 ka, which was used to infer decreasing strength of summer monsoon winds [*Gupta et al.*, 2003]. Another productivity record (using Ba/Al ratios from *Neogloboquadrina dutertrei*) off the Somali coast (Figure 1, green star NIOP-905) also implies decreased upwelling from 10 ka to present [*Ivanochko et al.*, 2005]. On land, speleothem records in Oman from the Hoti Cave [*Neff et al.*, 2001; *Fleitmann et al.*, 2003, 2007], Qunf Cave [*Fleitmann et al.*, 2003, 2007], and Defore Cave [*Fleitmann et al.*, 2007] suggest a more intense rainfall during early Holocene but decreasing monsoon strength during the middle to late Holocene (Figure 1, orange diamonds).

3. Data Used in Reconstructions

3.1. Paleo-SST Data

We exploit two common paleoproxy records for SSTs: (1) magnesium/calcium (Mg/Ca) ratios derived from isotopic analysis of planktonic foraminifera, such as *Globigerinoides ruber* [e.g., *Lea et al.*, 1999; *Nürnberg et al.*, 1996] and (2) an index of unsaturation ($U_{37}^{k'}$) derived from alkenones, which are produced by some species of coccolithophores, such as *Emiliana huxleyi* [e.g., *Brassell et al.*, 1986; *Herbert*, 2003]. *Gill et al.* [2016] offer more information on the use of these proxies within the reconstruction framework that we employ.

Our database consists of 39 (19 Mg/Ca and 20 $U_{37}^{k'}$) paleoproxy records of SSTs that span all or some portion of the past 10 ka and were collected from the National Oceanic and Atmospheric Administration (NOAA) National Center for Environmental Information (NCEI, formerly NCDC) paleoclimatology data set (http://www.ncdc.noaa.gov/data-access/paleoclimatology-data/datasets) and Pangaea (http://www.pangaea.de) for the equatorial Pacific, specifically 10°N to 10°S and 100°E to 60°W. These records were originally published using a variety of calibration equations. To combine all proxies into a single reconstruction, we recalibrated all the

records using a single Mg/Ca and a single $U_{37}^{k'}$ calibration using the *Dekens et al.* [2002] and *Müller et al.* [1998] calibrations, respectively, which are given as follows:

$$Mg/Ca = 0.33\exp 0.09 \left[SST(°C) + 0.042 \left(\Delta CO_3^{2-} \right) \right] \qquad (1)$$

$$U_{37}^{k'} = 0.033 * SST(°C) + 0.044 \qquad (2)$$

where ΔCO_3^{2-} represents the modern difference between the in situ concentration and the saturation concentration of carbonate ion, which helps to account for partial dissolution. Following recalibration, we smoothed all records using a local polynomial method with a second-order polynomial and a local neighborhood consisting of 70% of the nearest data points [e.g., *Loader*, 1996]. These records were then converted to SST anomalies using the 0 ka temperature from each smoothed record. Since anomalies are calculated using the 0 ka value, we excluded all records that did not extend to at least 2 ka prior to smoothing. Additionally, in some cases, there exists a Mg/Ca and $U_{37}^{k'}$ record for the same grid point. In these cases, we chose the proxy record that had the greater temporal resolution. After these exclusions, our final data set consists of 27 equatorial Pacific proxy records (west Pacific: 10 Mg/Ca and 4 $U_{37}^{k'}$; east Pacific: 4 Mg/Ca and 9 $U_{37}^{k'}$; Table A1). To view the time series in the original data set and to obtain details on excluded records, please refer to *Gill et al.* [2016].

3.2. Modern Data

Contemporary (1901–2013) gridded (2° by 2°) monthly SSTs were obtained from the NOAA NCEI Extended Reconstruction Sea Surface Temperature (ERSST) version 3b data set [*Smith et al.*, 2008] at all 27 locations where a paleo-SST record exists. We calculated contemporary monthly gridded (1.875° by 1.875°) wind stress curl (10^{-8} kg m^{-2} s^{-2}) using NOAA NCEP-NCAR CDAS-1 zonal and meridional momentum flux data for the period 1949–2013 [*Kalnay et al.*, 1996] and masked to include the surface wind stress curl only over tropical and north Arabian Sea grid cells (6.7°S to 31.4°N and 35.6°E to 76.9°E). Monthly anomalies were calculated for each data set using the 1981–2010 climatology. We then converted monthly SST anomalies to annual averages by averaging from May to the following April in order to capture the annual ENSO cycle. Summer wind stress curl anomalies were calculated by averaging June, July, August, and September anomalies. We obtained daily gridded (1° by 1°) rainfall from the India Meteorological Department [*Rajeevan et al.*, 2006]. We created an average daily summer monsoon rainfall (mm d^{-1}) time series for each grid cell by averaging the daily totals from 1 June to 30 September over the 1901–2004 period.

During the summer season, SSTs over northern Indian Ocean (Arabian Sea and Bay of Bengal) are modulated by the monsoon [*Krishnamurthy and Kirtman*, 2003], wherein strong winds enable cooler SSTs from coastal upwelling and evaporative cooling. Therefore, reconstructing the winds obviates the need for SST reconstructions. Indian Ocean SSTs exhibit a well-documented [e.g., *Allan et al.*, 1995; *Ihara et al.*, 2008; *Roxy et al.*, 2014; *Terray and Dominiak*, 2005] recent warming trend commonly attributed to anthropogenic sources. This warming trend, which might have been imparted to the wind stress curl, must be removed so that only the nonanthropogenic variability is reconstructed. To this end, first, a principal component analysis (PCA) of 1949–2013 ERSST over the Indian Ocean was performed and as expected the first orthogonal mode accounts for nearly 70% of the total variability in the data and is characterized by a strong warming trend (Figure B1). The eigenvalue spectrum (Figure B1) reveals that each of the remaining modes, however, explains only a small fraction of the remaining variance. Thus, we regress summer wind stress curl at each of the 262 grid points over the Arabian Sea against the first principal component (PC) of SSTs. The residuals from the regression represent the detrended wind stress curl time series at each grid point containing the nonanthropogenic variability.

4. Methodology

Interannual variability of monsoonal winds and Indian summer rainfall is influenced by the Walker Circulation, which is directly affected by equatorial Pacific SSTs [e.g., *Krishna Kumar et al.*, 1995; *Parthasarathy and Pant*, 1985; *Shukla and Mooley*, 1987; *Shukla and Paolino*, 1983; *Webster*, 1987; *Webster et al.*, 1998]. Therefore, to determine variations in monsoon strength throughout the Holocene, we use SST proxy records from the equatorial Pacific to reconstruct anomalies both in Arabian Sea summer wind stress curl and in monsoon rainfall over India. The reconstruction methodology consists of two key steps on the contemporary fields. First, we employ a PCA to isolate a small number of leading modes of variability in the contemporary "limited SST field" (i.e., SSTs at the locations of the proxy data) and the full contemporary climate field of the variable we desire to reconstruct for during Holocene time (i.e., summer wind stress curl over the Arabian Sea and summer monsoon precipitation over India). Second, we use a Canonical Correlation Analysis (CCA) following

Barnett and Preisendorfer [1987] to obtain the best relationship between the modes of the full field and that of the limited SST field during contemporary time. Then we use these relationships along with the paleoproxy SST data to reconstruct the modes of variability and, consequently, the spatial field of the summer wind stress curl and Indian monsoon precipitation during the Holocene. *Von Storch and Zwiers* [2001] provide details of PCA and CCA techniques.

The approach is based on the methodologies and assumptions of *Mann et al.* [1998]. A schematic of the reconstruction details is shown in Figure 3, which uses the summer wind stress curl reconstruction as an example and is described in section 4.1. The rainfall reconstruction follows that of wind stress curl closely and is discussed in section 4.2. We use boldfaced uppercase variables to denote matrices, with brackets used only when specifying the dimensions of the matrix and lowercase boldfaced variables to denote vectors. Calibration and verification results are in Appendix B. For a full description of the reconstruction methods and formulas, we refer readers to *Gill et al.* [2016] where we used the same method to reconstruct SSTs and zonal winds over equatorial Pacific during the past 10,000 years.

4.1. Reconstruction of Summer Monsoon Wind Stress Curl Fields

Recall that the trend from warming of Indian Ocean SSTs (Figure B1 was removed from the Arabian Sea wind stress curl data before performing the reconstruction. The contemporary detrended full field summer wind stress curl is then organized into a matrix, C of dimension $N \times G$, where N (= 65) is the number of years (1949–2013) and G (= 262) is the number of grid points.

Step (i). A principal component analysis (PCA) is performed on the wind stress curl field over Arabian Sea, which decomposes the curl data into principal components (PCs), Y, and eigenvectors, U. The first four PCs of the wind stress curl field account for 22.1%, 10.6%, 9.7%, and 8.9%, respectively, of the total variance of the field (for eigenvalue spectra see Appendix B and Figure B2). The spatial patterns of these modes—empirical orthogonal functions (EOFs) and PCs—are shown in Figure 4. The first EOF of the wind stress curl (22.1% of variance) shows large opposite values between the north/northwest and south/southeast sides of the monsoon jet, extending from the Somali coast to the western coast of India. The second wind stress curl EOF (10.6% of the variance) indicates a region of high variance that is concentrated on the eastern side of the Arabian Sea just off the west coast of India. The largest amplitude of the third EOF is near the equator. It is possible that the fourth EOF, which shows a region of high variability that extends to India farther north than the first EOF, is indicative of latitudinal shifts in the monsoon jet axis.

Step (ii). The contemporary limited field SST data at the locations of paleoproxy data, which extend across the equatorial Pacific region, are organized as a matrix, $T^\dagger$, of dimension $N \times P$, where N (= 65) is the length of the contemporary time period as before (1949–2013) and P (= 27) is the number of paleoproxy records. A PCA on this limited SST field decomposes the data into PCs, $Y^\dagger$, and eigenvectors, $U^\dagger$, and reveals that the first four modes of the limited equatorial Pacific SST field account for 82.1%, 11.3%, 1.5%, and 1.4% of the limited field variance (Figure B2).

Step (iii). We retain a small number of PCs (N_{PC}) from the contemporary full field PCA (Step i) and the limited field PCA (Step ii). To determine the optimal number of PCs to retain, we compared the calibration statistics across a number of scenarios that involved retaining PCs that explain no less than 5% of the variance. Considering this criterion, N_{PC} = 8 (75.5% of the full field variance) for summer wind stress curl. A Canonical Correlation Analysis (CCA) was performed on the first eight retained PCs of wind stress curl with the first eight PCs of the limited SST field, which decomposes the PCs of each field into a matrix of canonical components (CCs; denoted as S for curl and $S^\dagger$ for limited field SSTs) and a transformation matrix (A for curl; B for limited SSTs)). Each of the eight pairs of canonical components explains more of the joint variance than the next and is highly correlated with the other of the pair. For example, the correlation coefficient of the first CC of wind stress curl with the first CC of the limited SST field is 0.81. Each CC of the full wind stress curl field is then linearly regressed with the corresponding CC of the limited SST field. The solution to the least squares optimization, $\hat{\beta}$, will be used in Step v to reconstruct wind stress curl PCs.

Step (iv). For a given paleo time period (e.g., 10 ka), the smoothed proxy data, R, are contained in a $1 \times P$ matrix (where P is the number of proxy records that have values for the given reconstruction period). Using the transpose of the eigenvalue transformation matrix from the PCA in Step ii, $[U^\dagger]^T$, these proxy data are transformed into PCs, Y^R.

PCA on Contemporary Data

Steps i-ii: A PCA is performed on both the contemporary curl *[C]* and SST *[T†]* data, decomposing each into principal components *[Y]* and eigenvectors *[U]*.

1949-2013 JJAS wind stress curl
(*G* total points)

31°N

7°S
35°E   75°E

1949-2013 annual Pacific SSTs at
proxy locations (*P* total points)

10°N

10°S
100°E   60°W

$$\begin{bmatrix} C \end{bmatrix} = \begin{bmatrix} Y \end{bmatrix}\begin{bmatrix} U \end{bmatrix}$$
$$N \times G \quad\quad N \times G \quad\quad G \times G$$

$$\begin{bmatrix} T^{\dagger} \end{bmatrix} = \begin{bmatrix} Y^{\dagger} \end{bmatrix}\begin{bmatrix} U^{\dagger} \end{bmatrix}$$
$$N \times P \quad\quad N \times P \quad\quad P \times P$$

CCA

Step iii: The first few PCs (N_{PC}) from each are retained and a CCA is performed.

$$\begin{bmatrix} Y \end{bmatrix} = \begin{bmatrix} S \end{bmatrix}\begin{bmatrix} A \end{bmatrix}$$
$$N \times N_{PC} \quad\quad N \times N_{PC} \quad\quad N_{PC} \times N_{PC}$$

$$\begin{bmatrix} Y^{\dagger} \end{bmatrix} = \begin{bmatrix} S^{\dagger} \end{bmatrix}\begin{bmatrix} B \end{bmatrix}$$
$$N \times N_{PC} \quad\quad N \times N_{PC} \quad\quad N_{PC} \times N_{PC}$$

A regression is performed between each corresponding canonical component.

Proxy Data

Step iv: For a given paleo time-period (e.g. 10 ka), proxy data *[R]* are converted to PCs *[Y^{R}]* through eigenvector decomposition.

$$\begin{bmatrix} Y^{R} \end{bmatrix} = \begin{bmatrix} R \end{bmatrix}\begin{bmatrix} U^{\dagger} \end{bmatrix}^{T}$$
$$1 \times P \quad\quad 1 \times P \quad\quad P \times P$$

Reconstruction

Step v: Reconstructed PCs *[Ŷ]* are expanded by multiplication with canonical transformation matrix *[A]* and least squares optimization solution *[β]*. Means are used for remaining *G* minus N_{PC} PCs.

$$\begin{bmatrix} \hat{Y} \end{bmatrix} = \begin{bmatrix} Y^{R} \end{bmatrix}\begin{bmatrix} A \end{bmatrix}\begin{bmatrix} \beta \end{bmatrix}$$
$$1 \times N_{PC} \quad\quad 1 \times N_{PC} \quad\quad N_{PC} \times N_{PC} \quad\quad N_{PC} \times N_{PC}$$

Step vi: Reconstructed PCs are transformed to curl anomalies *[Ĉ]* through eigenvector expansion.

$$\begin{bmatrix} \hat{C} \end{bmatrix} = \begin{bmatrix} \hat{Y} \end{bmatrix}\begin{bmatrix} U \end{bmatrix}$$
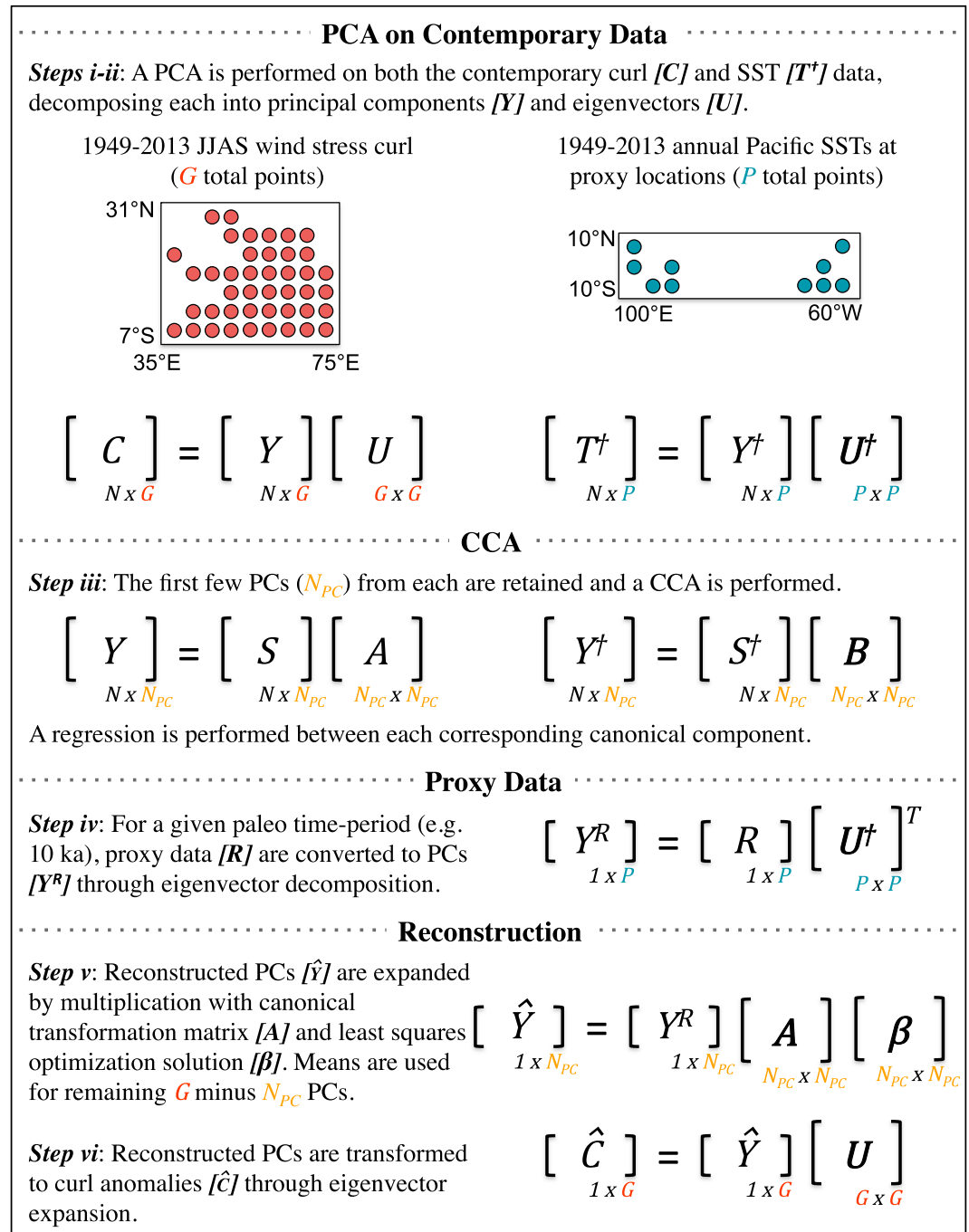$$1 \times G \quad\quad 1 \times G \quad\quad G \times G$$

Figure 3. A diagram of the main steps of the CCA reconstruction methodology for Arabian Sea summer wind stress curl. The steps are given for producing SSTs representative of 10 ka. Steps iii–vi are repeated for 8, 6, 4, and 2 ka. For the Indian summer rainfall reconstruction, the Steps i–vi are followed using contemporary rainfall instead of contemporary wind stress curl. The cross symbol denotes data, PCs, and transformation matrices associated with the limited field.

Step (v). Recall from Steps ii and iii that we retained N_{PC} CC's of the full field wind stress curl and limited field SSTs and formed regression relationships between the two fields. Reconstructed PCs, $\hat{Y}$, of the full 10 ka wind stress curl field are obtained through expansion by multiplication of the first N_{PC} proxy PCs, Y^{R}, (from Step v), with the canonical transformation matrix (*A*) from the canonical correlation and the least squares optimization solution ($\hat{\beta}$) from Step iii. In order to reconstruct the full field of the wind stress curl, we need the remaining (*G* minus N_{PC}) PCs. Since these capture less than 5% of the variance, we use the mean values from the PCs of
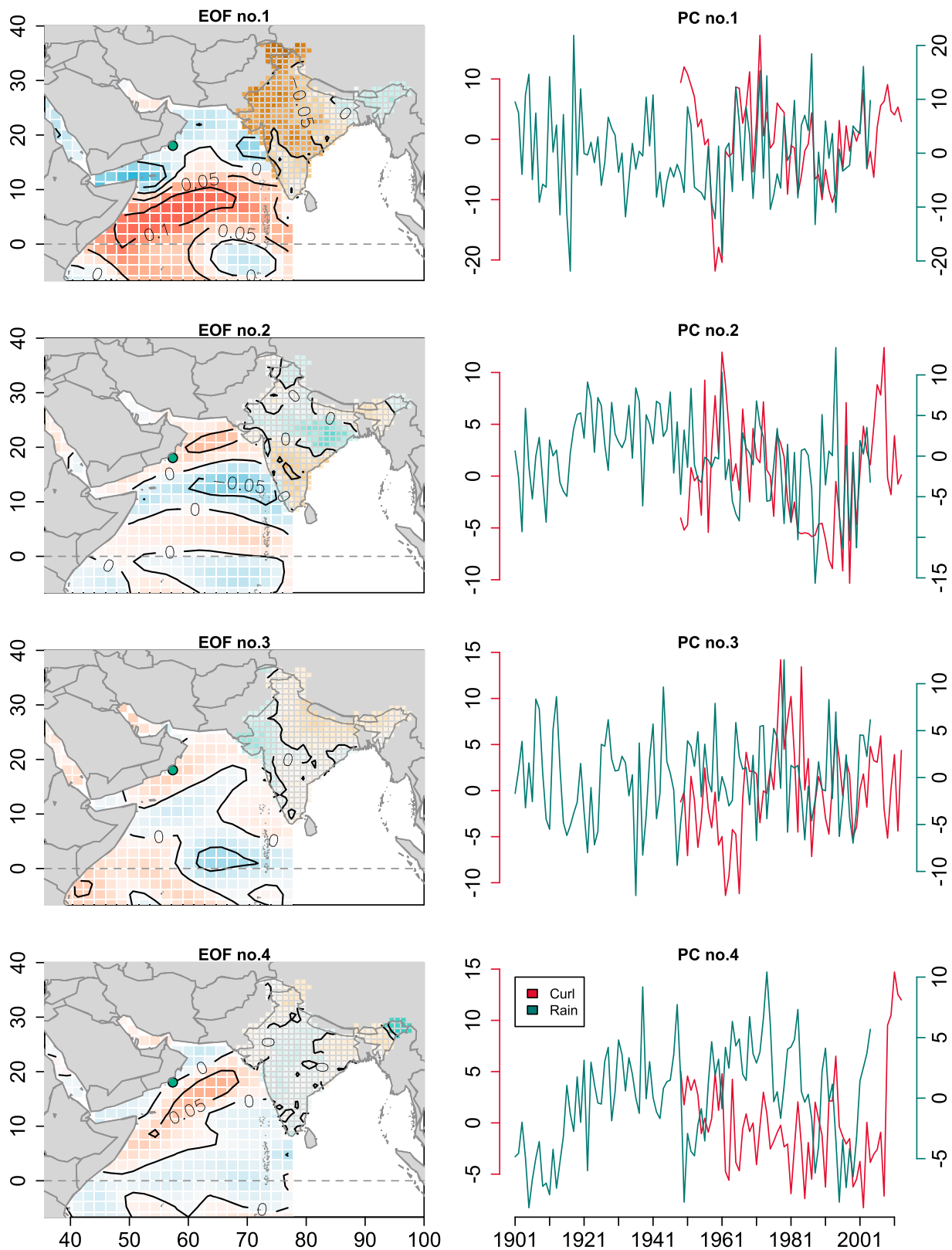
Figure 4. First four orthogonal EOFs and normalized PCs of Arabian Sea summer wind stress curl from 1994 to 2013 [*Kalnay et al.*, 1996] and Indian summer monsoon rainfall [*Rajeevan et al.*, 2006]. All EOFs are scaled by each eigenvalue associated with the mode. The green point off the coast of Oman indicates the location of the *Gupta et al.* [2003] *G. bulloides* record.

the contemporary period in Step i. This results in a full vector of PCs of wind stress curl of length G (= 262), corresponding to given paleo time period (e.g., 10 ka).

Step (vi). Finally, we back transform (convert reconstructions from PC-space to data-space) the reconstructed full field wind stress curl PCs, $\hat{Y}$, by multiplying them by the full field eigenvector matrix, U, which provides the full field reconstructions of wind stress curl anomalies, $\hat{C}$. Steps iii–vi are repeated for 8, 6, 4, and 2 ka.

4.2. Reconstruction of Summer Monsoon Rainfall Fields

For rainfall, the reconstruction process follows that for wind stress curl. There is no trend in the rainfall data that requires removal prior to the CCA reconstruction. We scale the seasonal average daily rainfall data (using means and standard deviations of each grid cell) and perform a PCA. The first four modes explain 18.3%, 7.8%, 5.9%, and 5.1% of the total field variance (Figure B2), and the corresponding EOFs and PCs are plotted on Figure 4. The first EOF of rainfall closely mimics the spatial pattern of the core monsoon region of India. The second EOF shows a pattern in which precipitation in the central and north India varies oppositely to that of south and northeast India. In the third, the split is longitudinal down the center of the country. Note that the first three PCs of rainfall vary similarly (in time) to the first three PCs of the wind stress curl field during the overlapping period of the two, which serves as evidence that these two fields are related.

The only difference in this methodology from that of the wind stress curl reconstruction is that N = 104 (for 1901–2004 data), G = 357 (grid cells over India), and we choose to retain the first four PCs (N_{PC} = 4) for the CCA, which jointly explain 37% of the variance. It should be underscored that this reconstruction focuses on capturing the variance present in the leading retained modes (i.e., the dominant "signal"). For rainfall, 37% of the total variance is captured. In other words, 37% of the variance is predictable. Although this may seem low compared to the percentage of the variance we were able to reconstruct in the wind stress curl field (76%), it is understandable given the spatial heterogeneity of rainfall. In fact, we argue that the ability that predicts 37% of the rainfall field is quite high given the variable nature of rainfall.

5. Results

5.1. Reconstruction of Holocene Summer Wind Stress Curl and Rainfall Fields

Reconstructions of Arabian Sea summer wind stress curl and Indian summer rainfall at 10, 6, 8, 4, and 2 ka are presented as percentage changes from the present-day (1981–2010) climatology (Figure 5). At 10 ka, the strongest positive anomalies in wind stress curl (upwelling), 30% greater than present day, are shown off the coast of Oman, extending and increasing to more than 50% greater than present day in the northeast region of the Arabian Sea. A band of negative anomalies in wind stress curl extends from the tip of the northern Somali coastline to the southern half of the Indian coastline, where wind stress curl anomalies were at least 50% less than present-day average wind stress curl. This general pattern of wind stress curl anomalies remains similar throughout the Holocene, but magnitudes gradually decrease from 8 to 6 ka. By 4 to 2 ka, both positive and negative anomalies are minimal, barely exceeding 1×10^{-8} kg m^{-2} s^{-2}.

Reconstructed rainfall patterns are consistent with the reconstructed summer wind stress curl. The 10 ka reconstruction suggests that compared to present day, (a) most of Rajasthan and northern India should have received 40% greater precipitation, with some areas experiencing up to 60% greater precipitation; (b) the regions of the Ganges and Godavari River Basins received about 15% greater precipitation; and (c) the rain shadow region east of the Western Ghats and North East India received less rainfall (~5–10% less than present day). Note that *Sukumar et al.* [1993] had inferred relatively arid conditions east of the Western Ghats when Rajasthan was wet. From 10 to 8 ka, this pattern changes little. By 6 ka, percentage differences in rainfall over Rajasthan and Northern India had decreased to 15–20% greater than present day, and since that time the central Ganges and Godavari regions remain at about 10% greater precipitation than present day. At 2 ka, precipitation across the core monsoon region (a spatial pattern similar to that of the first EOF of rainfall, e.g., Western Ghats and central and east-central India) does not exceed 10% greater than present day.

Although the strength of a CCA method derives from its ability to isolate dominant signals in a system, its biggest weakness is in dealing with uncertainties. Unfortunately, uncertainties in the reconstruction of PCs, eigenvalues, and eigenvectors cannot be robustly assessed. We quantify uncertainty on the PCs of the dominant signal by calculating the standard error between the signal for an observed period and the signal of the reconstruction. Standard errors in both wind stress curl and rainfall are small (within 2% of present-day values), which implies that the reconstruction of the signal is robust. We emphasize, however, that this represents the uncertainty in only the dominant signal, not the total uncertainty in the entire field.
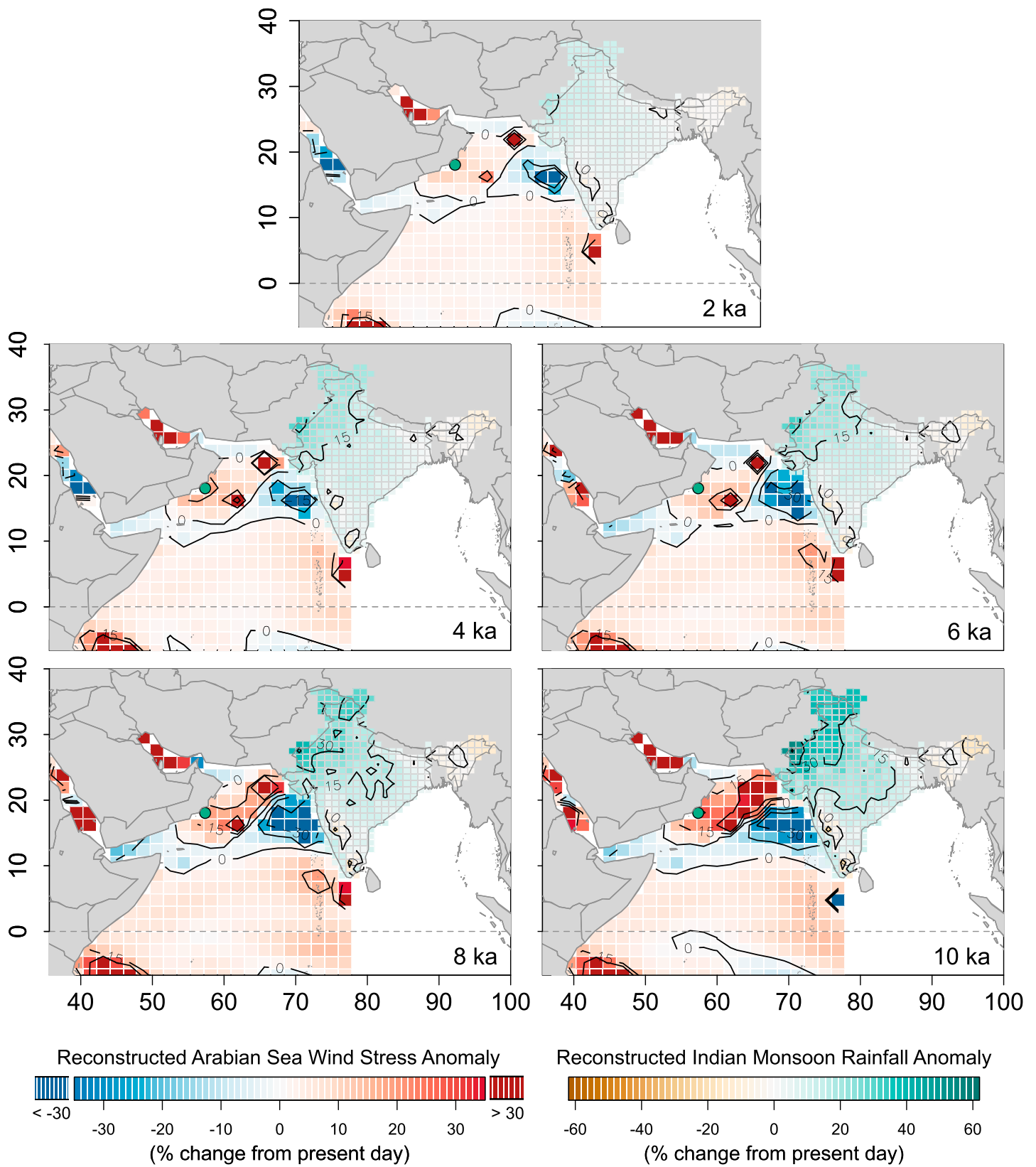
Figure 5. Reconstructed Arabian Sea summer wind stress curl anomalies and Indian summer monsoon rainfall for 10, 8, 6, 4, and 2 ka. Reconstructions are presented as percentage departures from the present day (1981–2010) climatology. The green point off the coast of Oman in the northwestern Arabian Sea indicates the location of the *G. bulloides* productivity/upwelling reconstruction provided by *Gupta et al.* [2003].
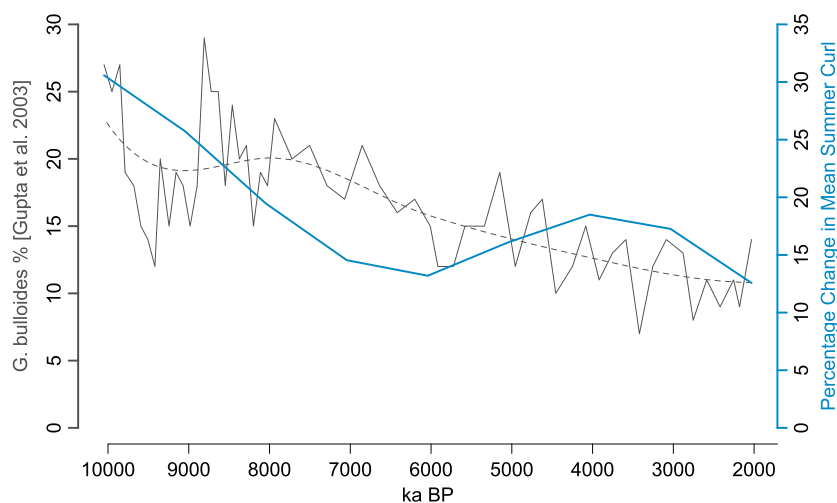
Figure 6. Comparison of the *Gupta et al.* [2003] reconstruction of *G. bulloides* percentage (black) to reconstructed percentage change in wind stress curl (blue) from 10 to 1 ka. A local polynomial is used to smooth the *G. bulloides* data and is provided by the dotted line.

As we alluded to before, there are multiple sources of uncertainty—assumption of stationarity of present-day teleconnection between equatorial Pacific SST gradient and the Indian Ocean wind stress and monsoon rainfall during Holocene, uncertainty in paleo-SST reconstructions, and last but not the least, the uncertainty in the present-day relationship. The uncertainty quantified above derives only from the reconstruction of the dominant signal.

5.2. Comparisons of Reconstructions to Proxy Records

Recall from the discussion of proxy records (section 2 and Figure 1) that a reconstruction of *G. bulloides* has been used to infer enhanced early Holocene upwelling off the coast of Oman (site OPD-732A), which suggests a weakening of the monsoon winds since 10 ka [*Gupta et al.*, 2003]. The interpretation of *G. bulloides* follows the logic that when the monsoon jet is strong, a large wind stress curl across the western Arabian Sea coastlines induces upwelling and a flux of cold nutrient-rich water to the surface, which favor *G. bulloides* over other planktonic foraminiferal species. Our reconstruction of wind stress curl is consistent with this record of *G. bulloides* as shown in Figure 6, which compares the *G. bulloides* time series of *Gupta et al.* [2003] to our reconstructed wind stress curl shown at the same location (Figure 5, green point). The smoothed *G. bulloides* record is the highest from ~10 to 8 ka, while the reconstructed wind stress curl is the highest at 10 and decreases monotonically until 7–6 ka. Wind stress curl increases slightly from 6 to 4 ka, before decreasing again to 2 ka. Although the millenial time scale variations of each time series do not align, the overall weakening trends are consistent.

Proxy data that suggest enhanced early to mid-Holocene rainfall over the Indian subcontinent tend to cluster in defined regions of India (Figure 1). For example, the majority of paleolake evidence in India comes from the northwestern region of Rajasthan (Figure 1, blue triangles). The northwestern region of India is also part of the Indus River Basin, which, by way of reconstructed discharge at core 63KA [*Staubwasser et al.*, 2003], is believed to have seen greater precipitation during the early Holocene. Our spatial reconstructions of rainfall reveal upward of 40–60% greater rainfall than at present over this region (Figure 5), which is consistent with the aforementioned proxy records. Other proxy records supporting a stronger monsoon fall in other regions of India. For instance, the sediment records (Figure 1, purple box) and north Bay of Bengal salinity record (Figure 1, 126KL) are presumably responding to changes in rainfall over the Indo-Gangetic Plains, which are located along the northeastern border of India. Additionally, the salinity record at the mouth of the Godavari River Basin (Figure 1, 16A) suggests enhanced rainfall over the central region of India.

With these various regions in mind, we define six regions over India, for which we reconstruct mean daily monsoon rainfall time series: Northern India, Rajasthan, Western Ghats, Indo-Gangetic Plains, NE India, and Godavari (Figure 7). For each region, mean 1901–2004 daily summer rainfall time series was averaged over the grid cells stippled in Figure 7. We then regressed these time series as functions of the first four limited SST field PCs (see Step ii in section 4). We used these functional relationships, along with the paleo-PCs
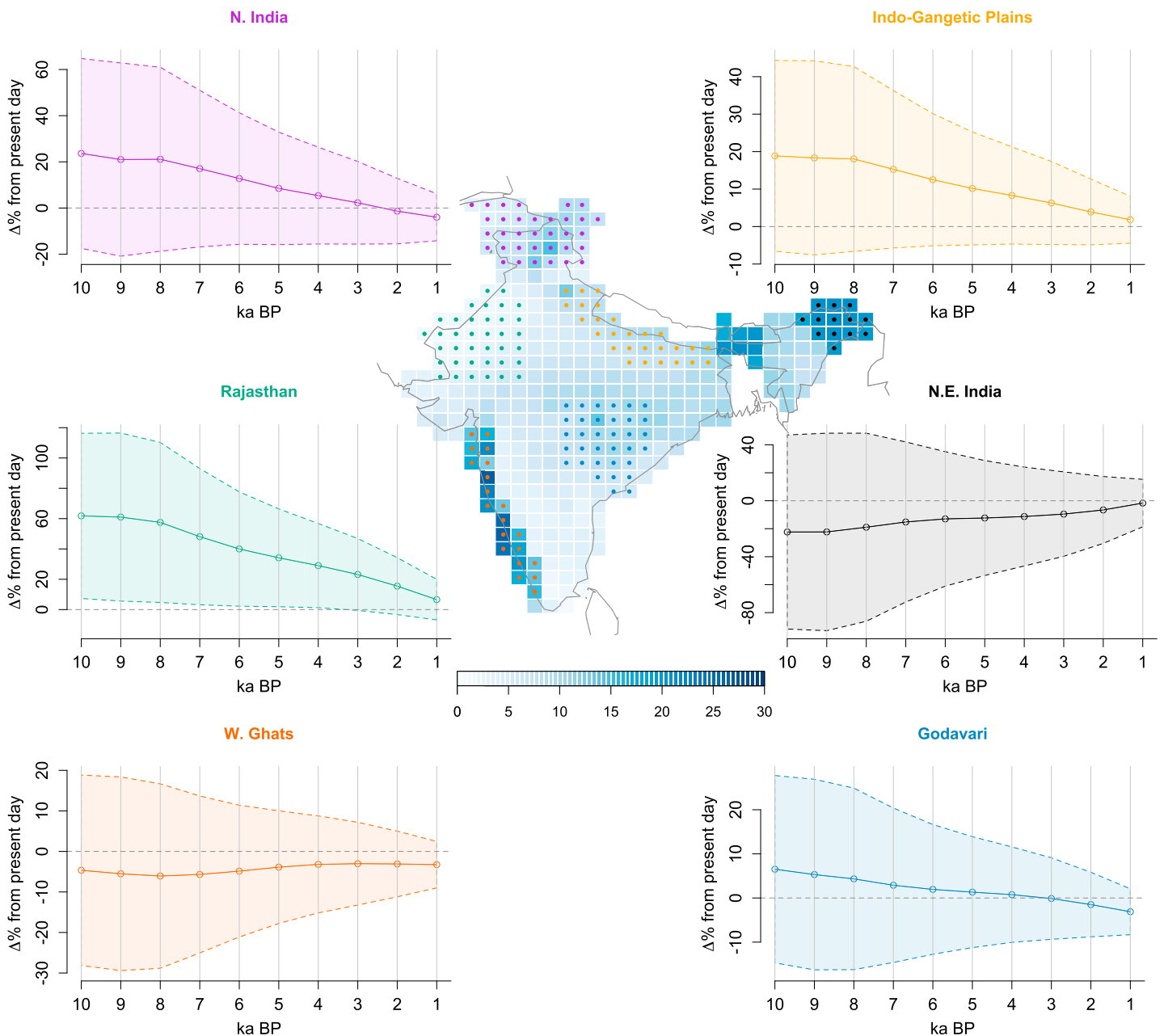
Figure 7. Reconstructed mean daily rainfall (mm d^{-1}) for the monsoon season for six regions: Northern India, Rajasthan, Western Ghats (green), Indo-Gangetic Plains, North East India, and Godavari River Basin. The stippled regions indicate the grid cells used for each respective reconstruction. Mean daily rainfall from 1901 to 2004 from *Rajeevan et al.* [2006] is shaded on the map. Rainfall is reconstructed by mean daily monsoon rainfall from each stippled region as a function of the limited field SST proxies. Shading on the time series represents the standard error from each regression.

(see Step iii in section 4), to predict rainfall for each 1000 year period from 10 to 1 ka (Figure 7). Standard errors from the regression model fit provide errors on the rainfall reconstructions.

Among interesting features, first, four of the regional reconstructions indicate greater precipitation during the early and mid-Holocene as compared to present day, which is also reflected in the spatial CCA reconstruction (Figure 5). Specifically, Rajasthan shows the greatest change, with 60% greater precipitation. A hydrological lake model [*Gill et al.*, 2015b] revealed that average annual precipitation 40–65% greater than present day was necessary to sustain Lake Sambhar in Rajasthan, India (Figure 1). Reconstructed spatial fields (Figure 5) and time series (Figure 7) for Rajasthan suggest that, although uncertainty is large, it is possible that ENSO teleconnections during an early to mid-Holocene La Niña-like state contributed enough summer rainfall to

Rajasthan to explain the enhanced wetness recorded by lake proxy records. Additionally, the Indo-Gangetic Plains and northern India show 20% greater precipitation from 10 to 8 ka, and Godavari shows just under 10% greater precipitation at 10 ka as compared to present day (Figure 7). This timing is consistent with proxy records representative of runoff from the Ganges River Basin: (1) *Kudrass et al.* [2001] cite a minimum in salinity from the early to mid-Holocene that gradually increases to present day, and (2) *Goodbred and Kuehl* [2000] cite the greatest sediment discharge between 11 and 7 ka. For the Godavari River Basin, *Ponton et al.* [2012] cite increased salinity in the past 3 ka.

The one record that shows the opposite (increasing) trend in rainfall since 10 ka is NE India, which is consistent with both the spatial reconstruction and also contemporary patterns. NE India is known to be out of phase with the rest of the core monsoon region in terms of interannual variability (see the first EOF of rainfall in Figure 4 and *Guhathakurta and Rajeevan* [2008]), in that its relationship with ENSO (higher rainfall during El Niño years) is opposite to that of the core monsoon region (lower rainfall during El Niño years). This reconstruction is consistent with present-day patterns and also with reconstructed records of pollen proxy data that span the past 12 ka [*Mehrotra et al.*, 2014]. Additionally, during the late Holocene when most of the proxy records from the core monsoon region suggest aridification, the estimated precipitation for Northeast India is near that of the present day, if not slightly above, which would be consistent with a return of ENSO variability. We would expect to see increased rainfall over the Western Ghats during the early Holocene, but instead, the reconstructed time series shows almost no change over the past 10 ka.

According to the definition of standard error, predictions closest to the mean carry the highest confidence. Thus, the uncertainties in rainfall reconstructions for each time series are large (see the shaded regions in the time series reconstructions in Figure 7), in part because the PC models must predict rainfall outside that of the observed range (far from the mean). In most cases, the large uncertainties make these trends marginally significant. At the least, these reconstructions suggest that it is possible for equatorial Pacific SSTs to externally force increased wetness over India.

6. Conclusions

A total of 27 proxy SST records (Mg/Ca and $U_{37}^{k'}$) that span the west and east equatorial Pacific is used in a reduced dimension methodology to reconstruct the full field dominant signal of Indian summer monsoon wind stress curl and rainfall at 10, 8, 6, 4, and 2 ka. The reconstructions reveal the greatest wind stress curl and rainfall anomalies, as compared to present day, at 10 ka. These anomalies weaken and lessen throughout the middle and late Holocene.

These reconstructions are consistent with a marine proxy record off the coast of Oman [*Gupta et al.*, 2003] that suggests enhanced upwelling during the early Holocene as compared to late Holocene. Additionally, average rainfall time series for the past 10 ka for six regions throughout India (Northern India, Rajasthan, Western Ghats, Indo-Gangetic Plains, Northeast India, and the Godavari Basin) are reconstructed using the PCs from the limited SST field. The rainfall reconstructions are consistent with many marine and continental proxy records that suggest enhanced rainfall during the early to mid-Holocene as compared to late Holocene. Although most rainfall time series reconstructions suggest the greatest precipitation at 10 ka, they reveal slight differences in the timing of each region that can be applied to various proxy records for precipitation and monsoon strength that have been reconstructed across the Indian subcontinent (Figure 1).

Gill et al. [2016] showed that when combining Mg/Ca and $U_{37}^{k'}$ in a reduced-dimension reconstruction, reconstructed equatorial Pacific SSTs and zonal winds suggest an enhanced La Niña-like state that was greatest at 10 ka, and the eastern equatorial Pacific gradually warmed to 2 ka. The significance of the monsoon reconstruction lies in the fact that only the patterns of wind stress curl and rainfall tied to equatorial Pacific SSTs are reconstructed. Therefore, although these findings do not consider the role of direct radiative forcing (due to insolation) over India on winds and rainfall during the early Holocene, they imply that it is possible that teleconnections from the tropical Pacific wrote a dominant signal on early to mid-Holocene Indian monsoon wetness. In other words, a stronger Indian summer monsoon can be explained by the type of variability experienced during the past century due to the monsoon-ENSO teleconnection. Accordingly, a warmer late Holocene Pacific might be responsible for the aridification over India at that time.

Many GCM studies have attributed an enhancement of early to mid-Holocene Indian summer monsoon [e.g., *Bosmans et al.*, 2012; *Braconnot et al.*, 2002, 2007a, 2007b, 2008; *Brown et al.*, 2008; *de Noblet et al.*, 1996;

Table A1. A List of the Mg/Ca and Uk'37 Proxy Records From the Equatorial Pacific That Were Used in the Reconstructions of Indian Summer Monsoon Climate Fields

Proxy	Core Name	Latitude	Longitude	Depth (m)	Original Calibration	Reference
			Western Equatorial Pacific			
Mg/Ca	MD01 - 2390	6.64	113.41	1545	*Dekens et al.* [2002]	*Steinke et al.* [2008]
Mg/Ca	MD98 - 2181	6.30	125.83	2114	*Nürnberg et al.* [1996]	*Stott et al.* [2004]
Mg/Ca	GeoB 10029-4	−1.50	100.10	964	*Anand et al.* [2003]	*Mohtadi et al.* [2010]
Mg/Ca	MD98 - 2162	−4.69	117.90	1855	*Hastings et al.* [2001]	*Visser et al.* [2003]
Mg/Ca	70 GGC	−3.56	119.40	482	*Anand et al.* [2003]	*Linsley et al.* [2010]
Mg/Ca	MD98 - 2176	−5.00	133.45	2382	*Nürnberg et al.* [1996]	*Stott et al.* [2004]
Mg/Ca	GeoB 10038-4	−5.90	103.30	1819	*Anand et al.* [2003]	*Mohtadi et al.* [2010]
Mg/Ca	13 GGC	−7.40	115.20	594	*Anand et al.* [2003]	*Linsley et al.* [2010]
Mg/Ca	MD98 - 2165	−9.65	118.34	2100	*Dekens et al.* [2002]	*Levi et al.* [2007]
Mg/Ca	MD98 - 2170	−10.59	125.39	832	*Nürnberg et al.* [1996]	*Stott et al.* [2004]
$U^{k'}_{37}$	GIK 18252-3	9.23	109.38	1273	*Pelejero and Grimalt* [1997]	*Kienast et al.* [2001]
$U^{k'}_{37}$	MD97 - 2151	8.72	109.87	1598	*Pelejero and Grimalt* [1997]	*Zhao et al.* [2006]
$U^{k'}_{37}$	GIK 17964	6.16	112.21	1556	*Müller et al.* [1998]	*Pelejero et al.* [1999]
$U^{k'}_{37}$	SO139 - 74KL	−6.54	103.83	1690	*Conte et al.* [2006]	*Lückge et al.* [2009]
			Eastern Equatorial Pacific			
Mg/Ca	ODP - 1242	7.86	−83.61	1364	*Anand et al.* [2003]	*Benway et al.* [2006]
Mg/Ca	TR163 - 22	0.52	−92.40	2830	*Dekens et al.* [2002]	*Lea et al.* [2006]
Mg/Ca	ODP - 1240	0.02	−86.45	2921	*Dekens et al.* [2002]	*Pena et al.* [2008]
Mg/Ca	V21 - 30	−1.22	−89.68	617	*Dekens et al.* [2002]	*Koutavas et al.* [2006]
$U^{k'}_{37}$	MD02 - 2529	8.21	−84.12	1619	*Sonzogni et al.* [1997]	*Leduc et al.* [2007]
$U^{k'}_{37}$	KNR176 - JPC32	4.85	−77.96	2200	*Prahl et al.* [1988]	*Pahnke et al.* [2007]
$U^{k'}_{37}$	TR163 - 19	2.25	−90.95	2348	*Prahl et al.* [1988]	*Dubois et al.* [2009]
$U^{k'}_{37}$	ME0005A - 24JC	1.50	−89.68	2941	*Prahl et al.* [1988]	*Kienast et al.* [2006]
$U^{k'}_{37}$	V19 - 27	−0.47	−82.67	1373	*Prahl et al.* [1988]	*Koutavas and Sachs* [2008]
$U^{k'}_{37}$	V19 - 28	−2.51	−84.65	2720	*Prahl et al.* [1988]	*Koutavas and Sachs* [2008]
$U^{k'}_{37}$	ME0005A - 27JC	−1.85	−82.78	2203	*Prahl et al.* [1988]	*Dubois et al.* [2009]
$U^{k'}_{37}$	V19 - 30	−3.38	−83.52	3091	*Prahl et al.* [1988]	*Koutavas and Sachs* [2008]
$U^{k'}_{37}$	CDH - 26	−3.59	−81.18	1023	*Prahl et al.* [1988]	*Bova et al.* [2015]

Joussaume et al., 1999; *Kitoh and Murakami*, 2002; *Liu et al.*, 2000, 2003, 2004; *Marzin and Braconnot*, 2009; *Marzin et al.*, 2013; *Zheng et al.*, 2008] and potentially all Northern Hemisphere monsoons [*Liu et al.*, 2003] to changes in insolation through direct radiative forcing. Although we separate the signature of a cooler Pacific from that of direct radiative forcing on the Indian summer monsoon, we acknowledge the consensus view that changes in orbital parameters reduced ENSO [e.g., *Cane et al.*, 2006] and thus cooled the Pacific. Suppressed ENSO variability has been demonstrated in many GCM studies [e.g., *Braconnot et al.*, 2012; *Brown et al.*, 2006; *Clement et al.*, 2000; *Liu et al.*, 2000; *Roberts et al.*, 2014; *Zheng et al.*, 2008] and attributed to (1) asymmetric heating of the tropical Pacific (warmer SST anomalies in the west than the east) in conjunction with Bjerkes feedback [*Clement et al.*, 2000], (2) enhanced monsoon winds intensifying Pacific trades and counteracting the development of SST anomalies [*Liu et al.*, 2000, 2003, 2004; *Zheng et al.*, 2008], or (3) a change in the weather in the extratropical Northern Hemisphere that supplies noise that typically excites ENSO [*Chiang et al.*, 2009; *Chiang and Fang*, 2010]. Whereas the first explanation relies on radiative forcing directly on the tropical Pacific, the latter two rely on forcing from climate changes outside of the tropical Pacific. Despite disagreement in how the Pacific cooled, we emphasize the possibility that the impact of insolation change on the monsoon was delivered through the dynamics of the earth climate system rather than directly through radiative (i.e., thermodynamic) forcing on the Indian subcontinent. In fact, a few of the aforementioned studies have explicitly linked the enhancement of the monsoon to larger climate dynamics resulting from shifted Hadley-Walker cells [e.g., *de Noblet et al.*, 1996; *Kitoh and Murakami*, 2002; *Zhao et al.*, 2005].

Appendix A: Tropical Pacific SST Proxy Records

This appendix, Table A1, provides information on the tropical Pacific SST proxy records that were used in the reconstructions and are mapped in blue in Figure 1 (bottom).

Appendix B: Details of Reconstruction Methods

This appendix provides further detail on the methods used to reconstruct wind stress curl and rainfall fields, including figures that display the trends in Indian Ocean SSTs, the eigenvalue spectra associated with each of the three principal component analyses performed, and the results of calibration and validation tests on the reconstruction method.

B1. Trend in Indian Ocean SSTs

A PCA on the wind stress curl field reveals that the first PC is a linear trend, which is undoubtedly due to the warming of the Indian Ocean that has occurred over the contemporary period. In order to remove the portion of the wind stress curl field trend that is only related to warming, we regressed the first PC of the Indian Ocean (Figure B1) against the wind stress curl and then proceeded with the reconstruction using the residuals only. This step ensured that we removed only the portion of the wind stress curl trend that was directly related to the SST warming trend.
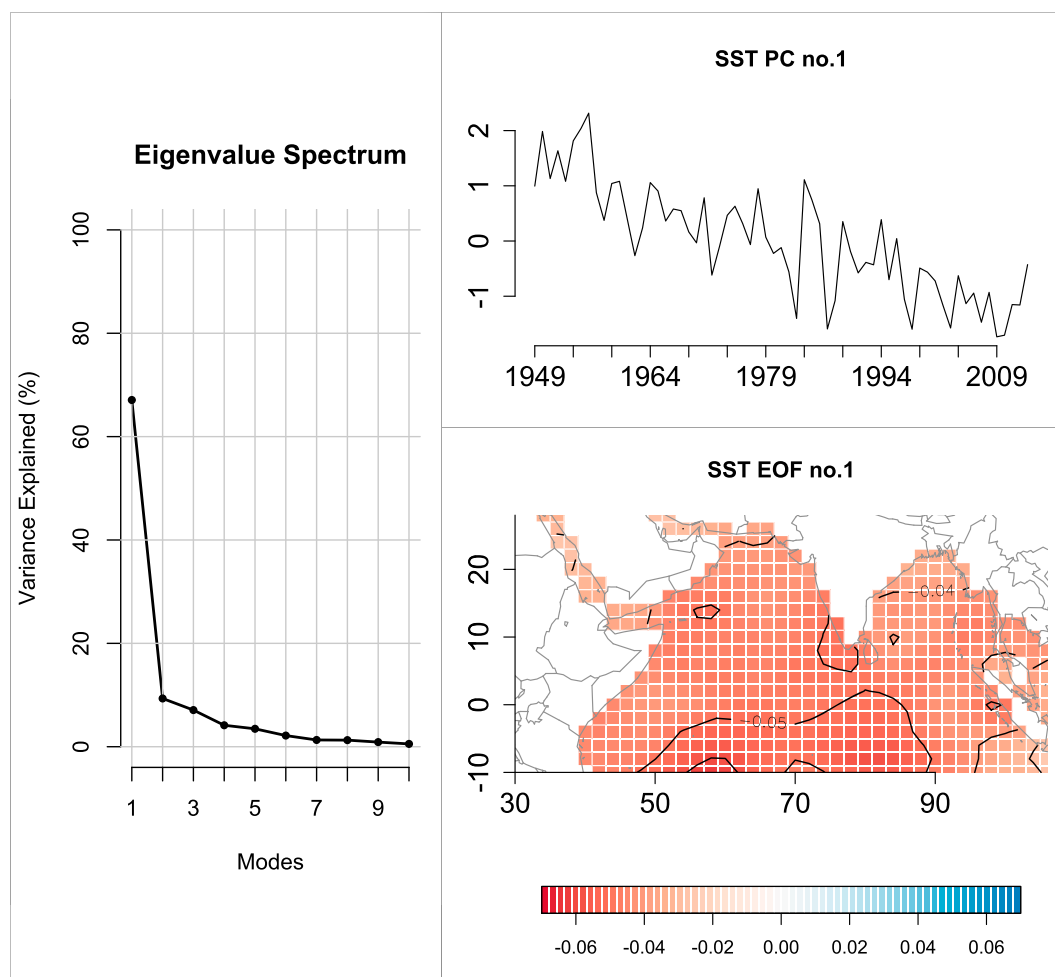
Figure B1. First orthogonal mode of summer (June–September) Indian Ocean SSTs from 1949 to 2013 [*Smith et al.*, 2008]. The eigenvalue spectrum on the left shows the percentage of variance explained by each of the first 10 orthogonal modes resulting from a PCA on Arabian Sea SSTs. The first mode accounts for nearly 70% of the total variance of the field. (top, right) The temporal PC and (bottom, right) the spatial EOF of the first most dominant mode are strong contemporary trends. The influence of this trend was removed from summer contemporary wind data prior to paleoreconstructions. The second and third modes explain 9% and 7% of the total variance, respectively. The fourth mode, and all modes after, each explain less than 5% of the total variance.
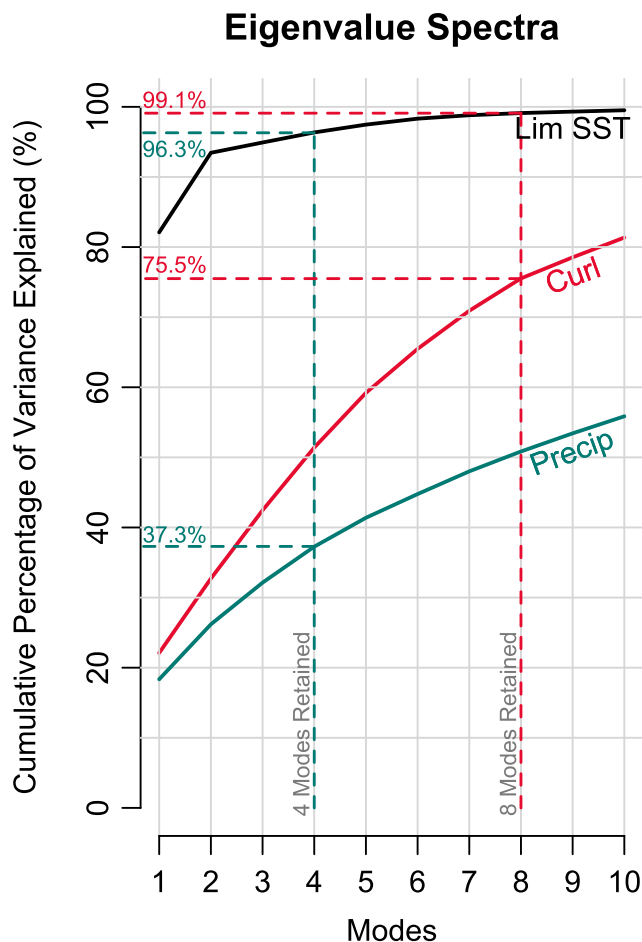
Figure B2. Eigenvalue spectrums (EVS) for the full field of Arabian Sea summer wind stress curl (1949–2013) [*Kalnay et al.*, 1996], full field of Indian summer monsoon rainfall (1901–2004) [*Rajeevan et al.*, 2006], and limited Indo-Pacific SST field (1949–2013) [*Smith et al.*, 2008]. These are color coded as red, green, and black, respectively. The eigenvalue spectra plot the cumulative percentage of variance explained by each additional mode retained. For example, the first eight orthogonal modes of wind stress curl were used for the reconstruction, which results in 75.5% of full field wind stress curl variance and 99.1% of limited SST field variance. Retaining the first four modes for the rainfall reconstruction resulted in 37.3% of variance for the full rain field and 96.3% of variance of the limited SST field variance.

B2. Eigenvalue Spectra

Eigenvalue spectra explain the percentage of variance that each mode explains. Given that a PCA was performed on the wind stress curl (red), rainfall (green), and limited SST (black) fields, we present those three respective eigenvalue spectra in Figure B2. The dotted lines indicate the number of modes retained for each of the two reconstructions and the resultant total percentage of variance explained: eight modes for the wind stress curl reconstruction (75.5% and 99.1% of the total variance in the wind stress curl and limited SST fields, respectively) and four modes for the rainfall reconstruction (37.3% and 96.3% of the total variance in the wind stress curl and limited SST fields, respectively).

B3. Model Calibration and Verification

As mentioned above, the reconstructions recover the dominant signal in the wind stress curl and rainfall fields, which account for a relatively small, but significant, percentage of the total variance. Thus, comparing the reconstructions to the full original data field will result in modest to poor skills. To be consistent, we compute the calibration and validation measures on the *signal component* of the original field. The signal component is obtained by projecting the PCs on to the retained eigenvectors. For example, let X be the original data matrix of size $N \times G$, Y be the matrix of all the principal components also of size $N \times G$ and, U_R be the reduced eigenvector matrix of size $G \times G$ with the first N_{PC} columns containing the eigenvectors of the first N_{PC} modes and zero for the rest. The signal component of the original data X_R is obtained as follows: $X_R = [Y][U_R]$.
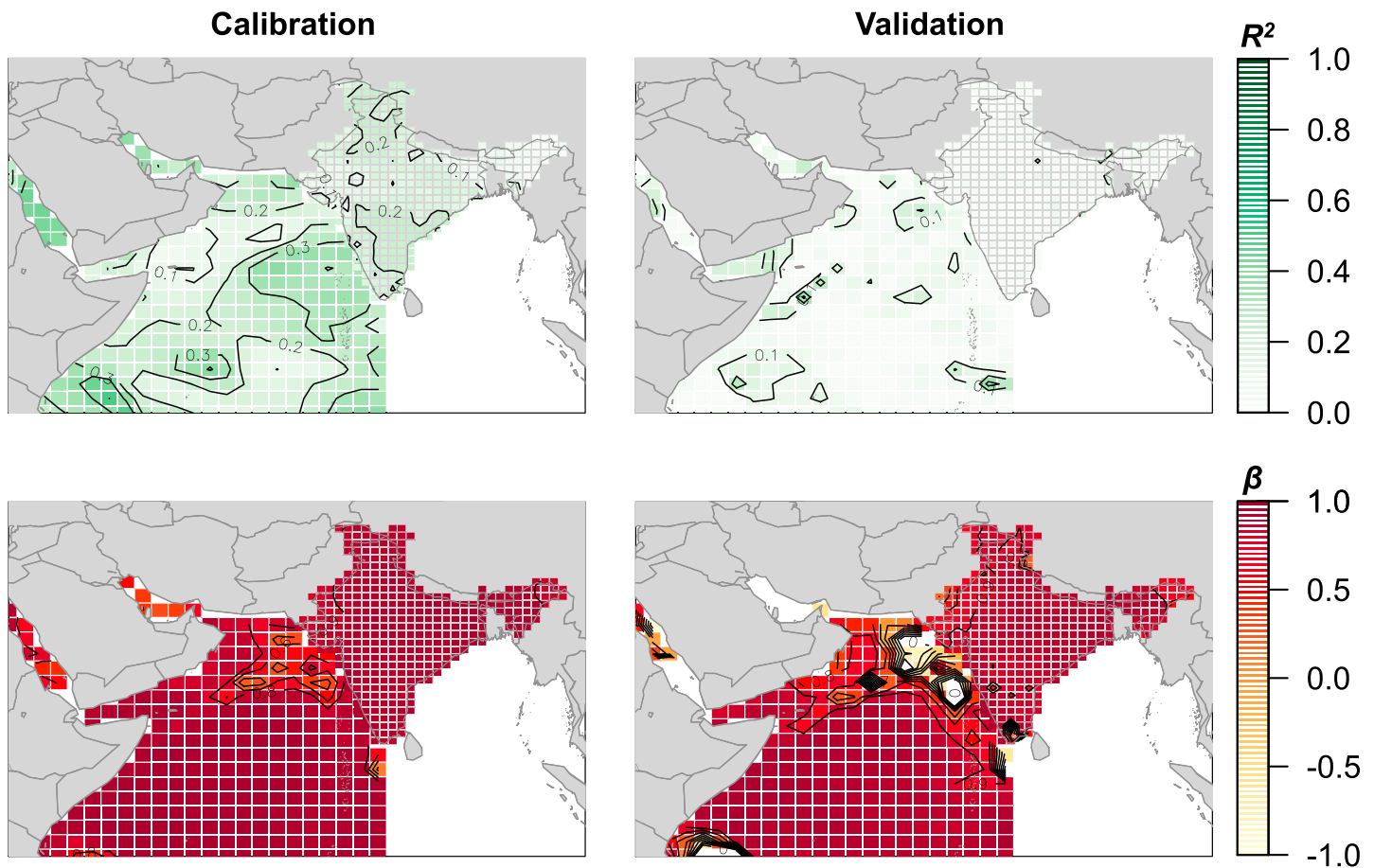
Figure B3. (left column) Model calibration and (right column) validation statistics for wind stress curl and rain for the CCA-based reconstruction models. Calibration statistics compare the reconstructed contemporary data to the actual contemporary data of each variable. In validation, we use the PCs of the modern period (post-1980) to reconstruct the PCs of the previous period (pre-1980). Thus, the validation statistics are comparing the reconstructed pre-1980 period to the actual pre-1980 period. The R^2 (top) provides the squared correlation coefficient and the β statistic (bottom) represents the resolved variance captured by the reconstructed data.

Model calibration is performed on the signal components at each grid point using the "resolved variance" statistic, β, given by the following:

$$\beta = 1 - \frac{\sum (y - \hat{y})^2}{\sum y^2} \tag{B1}$$

where y is the contemporary signal component obtained in $\boldsymbol{X_R}$ above and $\hat{y}$ is the reconstructed signal data for the full period. The β statistic serves as a measure of the resolved variance: for a perfect fit in which y is equal to $\hat{y}$, $\beta = 1$; for a bad fit in which y and $\hat{y}$ are not equal, $\beta = -1$. We also compared the squared correlation, R^2, between y and $\hat{y}$ at each grid point. These two statistics assess the reliability of the procedure in reproducing the contemporary signal data (see *Gill et al.* [2016] and *Mann et al.* [1998] for more details on these statistics).

In calibration experiments, the wind stress curl signal (first eight PCs) is captured well ($\beta \geq 0.5$) throughout most of the monsoon jet region (Figure B3, bottom left). The quality of reconstructions is perhaps better observed in the R^2 plot in regions where $R^2 > 0.25$ (Figure B3, top left). For rainfall reconstructions the variability of the rainfall signal (first four PCs) is slightly better captured than those for wind stress curl according to $\beta > 0.75$ but shows similar skill to wind stress curl in R^2 values.

For independent validation we fitted the modes using 1980–2013 for wind stress curl and 1980–2004 for rainfall and then reconstructed the signal for the earlier periods (1949–1979 for wind stress curl and 1901–1979 for rainfall). The verification maps for the two fields resemble the calibration maps (Figure B3, right column)

but with lesser skill. This is not surprising, as only the most recent trends are used to reconstruct past variability. For wind stress curl the validation skills are poor ($\beta < 0$) near the northwestern coast of India but are better for the rest of the Arabian Sea region. For rainfall, values of $\beta > 0.75$ skill across the country.

References

Achyuthan, H., J. Quade, L. Roe, and C. Placzek (2007), Stable isotopic composition of pedogenic carbonates from the eastern margin of the Thar Desert, Rajasthan, India, *Quat. Int.*, 162, 50–60.

Allan, R. J., J. A. Lindesay, and C. J. Reason (1995), Multidecadal variability in the climate system over the Indian Ocean region during the Austral summer, *J. Clim.*, 8(7), 1853–1873.

Anand, P., H. Elderfield, and M. H. Conte (2003), Calibration of Mg/Ca thermometry in planktonic foraminifera from a sediment trap time series, *Paleoceanography*, 18(2), 1050, doi:10.1029/2002PA000846.

Barnett, T., and R. Preisendorfer (1987), Origins and levels of monthly and seasonal forecast skill for United States surface air temperatures determined by canonical correlation analysis, *Mon. Weather Rev.*, 115(9), 1825–1850.

Beaufort, L., S. Kaars, F. Bassinot, and V. Moron (2010), Past dynamics of the Australian monsoon: Precession, phase and links to the global monsoon concept, *Clim. Past*, 6(5), 695–706.

Benway, H. M., A. C. Mix, B. A. Haley, and G. P. Klinkhammer (2006), Eastern Pacific warm pool paleosalinity and climate variability: 0–30 kyr, *Paleoceanography*, 21, PA3008, doi:10.1029/2005PA001208.

Bosmans, J., S. Drijfhout, E. Tuenter, L. Lourens, F. Hilgen, and S. Weber (2012), Monsoonal response to mid-Holocene orbital forcing in a high resolution GCM, *Clim. Past*, 8, 723–740.

Bova, S. C., T. Herbert, Y. Rosenthal, J. Kalansky, M. Altabet, C. Chazen, A. Mojarro, and J. Zech (2015), Links between eastern equatorial Pacific stratification and atmospheric CO$_2$ rise during the last deglaciation, *Paleoceanography*, 30, 1407–1424, doi:10.1002/2015PA002816.

Braconnot, P., et al. (2002), How the simulated change in monsoon at 6 ka BP is related to the simulation of the modern climate: Results from the paleoclimate modeling intercomparison project, *Clim. Dyn.*, 19(2), 107–121.

Braconnot, P., et al. (2007a), Results of PMIP2 coupled simulations of the mid-Holocene and last glacial maximum. Part 1: Experiments and large-scale features, *Clim. Past*, 3(2), 261–277.

Braconnot, P., et al. (2007b), Results of PMIP2 coupled simulations of the mid-Holocene and last glacial maximum. Part 2: Feedbacks with emphasis on the location of the ITCZ and mid-and high latitudes heat budget, *Clim. Past*, 3(2), 279–296.

Braconnot, P., C. Marzin, L. Grégoire, E. Mosquet, and O. Marti (2008), Monsoon response to changes in Earth's orbital parameters: Comparisons between simulations of the Eemian and of the Holocene, *Clim. Past Discuss.*, 4(2), 459–493.

Braconnot, P., Y. Luan, S. Brewer, and W. Zheng (2012), Impact of Earth's orbit and freshwater fluxes on Holocene climate mean seasonal cycle and ENSO characteristics, *Clim. Dyn.*, 38(5–6), 1081–1092.

Brassell, S., G. Eglinton, I. Marlowe, U. Pflaumann, and M. Sarnthein (1986), Molecular stratigraphy: A new tool for climatic assessment, *Nature*, 320, 129–133.

Brown, J., M. Collins, and A. Tudhope (2006), Coupled model simulations of mid-Holocene ENSO and comparisons with coral oxygen isotope records, *Adv. Geosci.*, 6, 29–33.

Brown, J., M. Collins, A. W. Tudhope, and T. Toniazzo (2008), Modelling mid-Holocene tropical climate and ENSO variability: Towards constraining predictions of future change with palaeo-data, *Clim. Dyn.*, 30(1), 19–36.

Bryson, R. A., and A. Swain (1981), Holocene variations of monsoon rainfall in Rajasthan, *Quat. Res.*, 16(2), 135–145.

Cane, M. A., P. Braconnot, A. Clement, H. Gildor, S. Joussaume, M. Kageyama, M. Khodri, D. Paillard, S. Tett, and E. Zorita (2006), Progress in paleoclimate modeling, *J. Clim.*, 19(20), 5031–5057.

Chazen, C. R., M. A. Altabet, and T. D. Herbert (2009), Abrupt mid-Holocene onset of centennial-scale climate variability on the Peru-Chile margin, *Geophys. Res. Lett.*, 36, L18704, doi:10.1029/2009GL039749.

Chiang, J., Y. Fang, and P. Chang (2009), Pacific climate change and ENSO activity in the mid-Holocene, *J. Clim.*, 22(4), 923–939.

Chiang, J. C., and Y. Fang (2010), Was the North Pacific wintertime climate less stormy during the mid-Holocene?, *J. Clim.*, 23(14), 4025–4037.

Clement, A., R. Seager, and M. Cane (1999), Orbital controls on the El Niño/Southern Oscillation and the tropical climate, *Paleoceanography*, 14(4), 441–456.

Clement, A. C., R. Seager, and M. A. Cane (2000), Suppression of El Niño during the mid-Holocene by changes in the Earth's orbit, *Paleoceanography*, 15(6), 731–737.

Conroy, J. L., J. T. Overpeck, J. E. Cole, T. M. Shanahan, and M. Steinitz-Kannan (2008), Holocene changes in eastern tropical Pacific climate inferred from a Galápagos lake sediment record, *Quat. Sci. Rev.*, 27(11), 1166–1180.

Conte, M. H., M.-A. Sicre, C. Rühlemann, J. C. Weber, S. Schulte, D. Schulz-Bull, and T. Blanz (2006), Global temperature calibration of the alkenone unsaturation index (Uk'37) in surface waters and comparison with surface sediments, *Geochem. Geophys. Geosyst.*, 7, Q02005, doi:10.1029/2005GC001054.

Curry, W., D. Ostermann, M. Guptha, and V. Ittekkot (1992), Foraminiferal production and monsoonal upwelling in the Arabian Sea: Evidence from sediment traps, *Geol. Soc. London Spec. Publ.*, 64(1), 93–106.

de Noblet, N., P. Braconnot, S. Joussaume, and V. Masson (1996), Sensitivity of simulated Asian and African summer monsoons to orbitally induced variations in insolation 126, 115 and 6 ka BP, *Clim. Dyn.*, 12(9), 589–603.

Dekens, P. S., D. W. Lea, D. K. Pak, and H. J. Spero (2002), Core top calibration of Mg/Ca in tropical foraminifera: Refining paleotemperature estimation, *Geochem. Geophys. Geosyst.*, 3(4), 1022, doi:10.1029/2001GC000200.

Deotare, B., M. Kajale, S. Rajaguru, S. Kusumgar, A. Jull, and J. Donahue (2004), Palaeoenvironmental history of Bap-Malar and Kanod playas of Western Rajasthan, Thar Desert, *J. Earth Syst. Sci.*, 113(3), 403–425.

Dubois, N., M. Kienast, C. Normandeau, and T. D. Herbert (2009), Eastern equatorial Pacific cold tongue during the Last Glacial Maximum as seen from alkenone paleothermometry, *Paleoceanography*, 24, PA4207, doi:10.1029/2009PA001781.

Emile-Geay, J., M. Cane, R. Seager, A. Kaplan, and P. Almasi (2007), El Niño as a mediator of the solar influence on climate, *Paleoceanography*, 22, PA3210, doi:10.1029/2006PA001304.

Enzel, Y., L. Ely, S. Mishra, R. Ramesh, R. Amit, B. Lazar, S. Rajaguru, V. Baker, and A. Sandler (1999), High-resolution Holocene environmental changes in the Thar Desert, Northwestern India, *Science*, 284(5411), 125–128.

Fleitmann, D., S. J. Burns, M. Mudelsee, U. Neff, J. Kramers, A. Mangini, and A. Matter (2003), Holocene forcing of the Indian monsoon recorded in a stalagmite from Southern Oman, *Science*, 300(5626), 1737–1739.

Fleitmann, D., et al. (2007), Holocene ITCZ and Indian monsoon dynamics recorded in stalagmites from Oman and Yemen (Socotra), *Quat. Sci. Rev.*, 26(1), 170–188.

Gill, E., B. Rajagopalan, and P. Molnar (2015a), Subseasonal variations in spatial signatures of ENSO on the Indian summer monsoon from 1901 to 2009, *J. Geophys. Res. Atmos.*, *120*, 8165–8185, doi:10.1002/2015JD023184.

Gill, E., B. Rajagopalan, and P. Molnar (2015b), An assessment of the mean annual precipitation needed to sustain mid-Holocene lakes in Rajasthan, India, *Holocene*, *25*(12), 1923–1934.

Gill, E. C., B. Rajagopalan, P. Molnar, and T. M. Marchitto (2016), Reduced-dimension reconstruction of the equatorial pacific SST and zonal wind fields over the past 10,000 years using Mg/Ca and alkenone records, *Paleoceanography*, *31*, 928–952, doi:10.1002/2016PA002948.

Goodbred, S. L., and S. A. Kuehl (2000), Enormous Ganges-Brahmaputra sediment discharge during strengthened early Holocene monsoon, *Geology*, *28*(12), 1083–1086.

Guhathakurta, P., and M. Rajeevan (2008), Trends in the rainfall pattern over India, *Int. J. Climatol.*, *28*(11), 1453–1469.

Gupta, A. K., D. M. Anderson, and J. T. Overpeck (2003), Abrupt changes in the Asian Southwest monsoon during the Holocene and their links to the North Atlantic Ocean, *Nature*, *421*(6921), 354–357.

Hastings, D., M. Kienast, S. Steinke, and A. Whitko (2001), A comparison of three independent paleotemperature estimates from a high resolution record of deglacial SST records in the Tropical South China Sea, *Eos Trans. AGU*, *82*(47), Fall Meet. Suppl., Abstract PP12B–10.

Herbert, T. (2003), Alkenone paleotemperature determinations, in *Treatise on Geochemistry*, vol. 6, edited by H. Elderfield, H. D. Holland, and K. Turekian, pp. 391–432, Elsevier, Amsterdam.

Ihara, C., Y. Kushnir, and M. A. Cane (2008), Warming trend of the Indian ocean SST and Indian Ocean dipole from 1880 to 2004, *J. Clim.*, *21*(10), 2035–2046.

Ivanochko, T. S., R. S. Ganeshram, G.-J. A. Brummer, G. Ganssen, S. J. Jung, S. G. Moreton, and D. Kroon (2005), Variations in tropical convection as an amplifier of global climate change at the millennial scale, *Earth Planet. Sci. Lett.*, *235*(1), 302–314.

Joussaume, S., et al. (1999), Monsoon changes for 6000 years ago: Results of 18 simulations from the paleoclimate modeling intercomparison project (PMIP), *Geophys. Res. Lett.*, *26*(7), 859–862.

Kajale, M., and B. Deotare (1997), Late quaternary environmental studies on salt lakes in Western Rajasthan, India: A summarised view, *J. Quat. Sci.*, *12*(5), 405–412.

Kalnay, E., et al. (1996), The NCEP/NCAR 40-year reanalysis project, *Bull. Am. Meteorol. Soc.*, *77*(3), 437–471.

Kaplan, A., M. A. Cane, Y. Kushnir, A. C. Clement, M. B. Blumenthal, and B. Rajagopalan (1998), Analyses of global sea surface temperature 1856–1991, *J. Geophys. Res.*, *103*(C9), 18,567–18,589.

Kienast, M., S. Steinke, K. Stattegger, and S. Calvert (2001), Synchronous tropical South China Sea SST change and Greenland warming during deglaciation, *Science*, *291*(5511), 2132–2134.

Kienast, M., S. S. Kienast, S. E. Calvert, T. I. Eglinton, G. Mollenhauer, R. François, and A. C. Mix (2006), Eastern Pacific cooling and Atlantic overturning circulation during the last deglaciation, *Nature*, *443*(7113), 846–849.

Kitoh, A., and S. Murakami (2002), Tropical Pacific climate at the mid-Holocene and the last glacial maximum simulated by a coupled ocean-atmosphere general circulation model, *Paleoceanography*, *17*(3), 1047, doi:10.1029/2001PA000724.

Koutavas, A., and J. P. Sachs (2008), Northern timing of deglaciation in the Eastern Equatorial Pacific from alkenone paleothermometry, *Paleoceanography*, *23*, PA4205, doi:10.1029/2008PA001593.

Koutavas, A., J. Lynch-Stieglitz, T. M. Marchitto, and J. P. Sachs (2002), El Niño-like pattern in ice age tropical Pacific sea surface temperature, *Science*, *297*(5579), 226–230.

Koutavas, A., P. B. Demenocal, G. C. Olive, and J. Lynch-Stieglitz (2006), Mid-Holocene El Niño–Southern Oscillation (ENSO) attenuation revealed by individual foraminifera in eastern tropical Pacific sediments, *Geology*, *34*(12), 993–996.

Krishna Kumar, K., M. Soman, and K. R. Kumar (1995), Seasonal forecasting of Indian summer monsoon rainfall: A review, *Weather*, *50*(12), 449–467.

Krishna Kumar, K., B. Rajagopalan, M. Hoerling, G. Bates, and M. Cane (2006), Unraveling the mystery of Indian monsoon failure during El Niño, *Science*, *314*(5796), 115–119.

Krishna Kumar, K., K. Kamala, B. Rajagopalan, M. P. Hoerling, J. K. Eischeid, S. Patwardhan, G. Srinivasan, B. Goswami, and R. Nemani (2011), The once and future pulse of Indian monsoonal climate, *Clim. Dyn.*, *36*(11–12), 2159–2170.

Krishnamurthy, V., and B. P. Kirtman (2003), Variability of the Indian Ocean: Relation to monsoon and ENSO, *Q. J. R. Meteorol. Soc.*, *129*(590), 1623–1646.

Kudrass, H., A. Hofmann, H. Doose, K. Emeis, and H. Erlenkeuser (2001), Modulation and amplification of climatic changes in the Northern Hemisphere by the Indian summer monsoon during the past 80 ky, *Geology*, *29*(1), 63–66.

Kutzbach, J., and B. Otto-Bliesner (1982), The sensitivity of the African-Asian monsoonal climate to orbital parameter changes for 9000 years BP in a low-resolution general circulation model, *J. Atmos. Sci.*, *39*(6), 1177–1188.

Kutzbach, J. E. (1981), Monsoon climate of the early Holocene: Climate experiment with the Earth's orbital parameters for 9000 years ago, *Science*, *214*(4516), 59–61.

Lea, D. W., T. A. Mashiotta, and H. J. Spero (1999), Controls on magnesium and strontium uptake in planktonic foraminifera determined by live culturing, *Geochim. Cosmochim. Acta*, *63*(16), 2369–2379.

Lea, D. W., D. K. Pak, C. L. Belanger, H. J. Spero, M. A. Hall, and N. J. Shackleton (2006), Paleoclimate history of Galapagos surface waters over the last 135,000 yr, *Quat. Sci. Rev.*, *25*(11), 1152–1167.

Leduc, G., L. Vidal, K. Tachikawa, F. Rostek, C. Sonzogni, L. Beaufort, and E. Bard (2007), Moisture transport across Central America as a positive feedback on abrupt climatic changes, *Nature*, *445*(7130), 908–911.

Leduc, G., R. Schneider, J.-H. Kim, and G. Lohmann (2010), Holocene and Eemian sea surface temperature trends as revealed by alkenone and Mg/Ca paleothermometry, *Quat. Sci. Rev.*, *29*(7), 989–1004.

Levi, C., L. Labeyrie, F. Bassinot, F. Guichard, E. Cortijo, C. Waelbroeck, N. Caillon, J. Duprat, T. de Garidel-Thoron, and H. Elderfield (2007), Low-latitude hydrological cycle and rapid climate changes during the Last Deglaciation, *Geochem. Geophys. Geosyst.*, *8*, Q05N12, doi:10.1029/2006GC001514.

Li, C., and M. Yanai (1996), The onset and interannual variability of the Asian summer monsoon in relation to land-sea thermal contrast, *J. Clim.*, *9*(2), 358–375.

Linsley, B. K., Y. Rosenthal, and D. W. Oppo (2010), Holocene evolution of the Indonesian throughflow and the western Pacific warm pool, *Nat. Geosci.*, *3*(8), 578–583.

Liu, Z., J. Kutzbach, and L. Wu (2000), Modeling climate shift of El Niño variability in the Holocene, *Geophys. Res. Lett.*, *27*(15), 2265–2268.

Liu, Z., B. Otto-Bliesner, J. Kutzbach, L. Li, and C. Shields (2003), Coupled climate simulation of the evolution of global monsoons in the Holocene, *J. Clim.*, *16*(15), 2472–2490.

Liu, Z., S. Harrison, J. Kutzbach, and B. Otto-Bliesner (2004), Global monsoons in the mid-Holocene and oceanic feedback, *Clim. Dyn.*, *22*(2–3), 157–182.

Loader, C. R. (1996), Local likelihood density estimation, *Ann. Stat.*, *24*(4), 1602–1618.

Lückge, A., M. Mohtadi, C. Rühlemann, G. Scheeder, A. Vink, L. Reinhardt, and M. Wiedicke (2009), Monsoon versus ocean circulation controls on paleoenvironmental conditions off Southern Sumatra during the past 300,000 years, *Paleoceanography*, *24*, PA1208, doi:10.1029/2008PA001627.

Mann, M. E., R. S. Bradley, and M. K. Hughes (1998), Global-scale temperature patterns and climate forcing over the past six centuries, *Nature*, *392*(6678), 779–787.

Marzin, C., and P. Braconnot (2009), Variations of Indian and African monsoons induced by insolation changes at 6 and 9.5 kyr bp, *Clim. Dyn.*, *33*(2–3), 215–231.

Marzin, C., P. Braconnot, and M. Kageyama (2013), Relative impacts of insolation changes, meltwater fluxes and ice sheets on African and Asian monsoons during the Holocene, *Clim. Dyn.*, *41*(9–10), 2267–2286.

Mehrotra, N., S. K. Shah, and A. Bhattacharyya (2014), Review of palaeoclimate records from Northeast India based on pollen proxy data of Late Pleistocene–Holocene, *Quat. Int.*, *325*, 41–54.

Mohtadi, M., S. Steinke, A. Lückge, J. Groeneveld, and E. C. Hathorne (2010), Glacial to Holocene surface hydrography of the tropical eastern Indian Ocean, *Earth Planet. Sci. Lett.*, *292*(1), 89–97.

Moy, C. M., G. O. Seltzer, D. T. Rodbell, and D. M. Anderson (2002), Variability of El Niño/Southern Oscillation activity at millennial timescales during the Holocene epoch, *Nature*, *420*(6912), 162–165.

Müller, P. J., G. Kirst, G. Ruhland, I. von Storch, and A. Rosell-Melé (1998), Calibration of the alkenone paleotemperature index Uk'37 based on core-tops from the Eastern South Atlantic and the global ocean (60N-60S), *Geochim. Cosmochim. Acta*, *62*(10), 1757–1772.

Neff, U., S. Burns, A. Mangini, M. Mudelsee, D. Fleitmann, and A. Matter (2001), Strong coherence between solar variability and the monsoon in Oman between 9 and 6 kyr ago, *Nature*, *411*(6835), 290–293.

Nürnberg, D., J. Bijma, and C. Hemleben (1996), Assessing the reliability of magnesium in foraminiferal calcite as a proxy for water mass temperatures, *Geochim. Cosmochim. Acta*, *60*(5), 803–814.

Pahnke, K., J. P. Sachs, L. Keigwin, A. Timmermann, and S.-P. Xie (2007), Eastern tropical Pacific hydrologic changes during the past 27,000 years from D/H ratios in alkenones, *Paleoceanography*, *22*, PA4214, doi:10.1029/2007PA001468.

Parthasarathy, B., and G. Pant (1985), Seasonal relationships between Indian summer monsoon rainfall and the Southern Oscillation, *J. Climatol.*, *5*(4), 369–378.

Pelejero, C., and J. O. Grimalt (1997), The correlation between the Uk'37 index and sea surface temperatures in the warm boundary: The South China Sea, *Geochim. Cosmochim. Acta*, *61*(22), 4789–4797.

Pelejero, C., J. O. Grimalt, S. Heilig, M. Kienast, and L. Wang (1999), High-resolution Uk'37 temperature reconstructions in the South China Sea over the past 220 kyr, *Paleoceanography*, *14*(2), 224–231.

Pena, L., I. Cacho, P. Ferretti, and M. Hall (2008), El Niño–Southern Oscillation-like variability during glacial terminations and interlatitudinal teleconnections, *Paleoceanography*, *23*, PA3101, doi:10.1029/2008PA001620.

Ponton, C., L. Giosan, T. I. Eglinton, D. Q. Fuller, J. E. Johnson, P. Kumar, and T. S. Collett (2012), Holocene aridification of India, *Geophys. Res. Lett.*, *39*, L03704, doi:10.1029/2011GL050722.

Prahl, F. G., L. A. Muehlhausen, and D. L. Zahnle (1988), Further evaluation of long-chain alkenones as indicators of paleoceanographic conditions, *Geochim. Cosmochim. Acta*, *52*(9), 2303–2310.

Prasad, S., S. Kusumgar, and S. Gupta (1997), A mid-late Holocene record of palaeoclimatic changes from Nal Sarovar— A palaeodesert margin lake in western India, *J. Quat. Sci.*, *12*, 153–159.

Prell, W., and W. Curry (1981), Faunal and isotopic indices of monsoonal upwelling-western Arabian Sea, *Oceanol. Acta*, *4*(1), 91–98.

R Core Team (2014), *R: A Language and Environment for Statistical Computing*, R Foundation for Stat. Comput., Vienna.

Rajagopalan, B., and P. Molnar (2013), Signatures of Tibetan Plateau heating on Indian summer monsoon rainfall variability, *J. Geophys. Res. Atmos.*, *118*, 1170–1178, doi:10.1002/jgrd.50124.

Rajeevan, M., J. Bhate, J. Kale, and B. Lal (2006), High resolution daily gridded rainfall data for the Indian region: Analysis of break and active monsoon spells, *Curr. Sci.*, *91*(3), 296–306.

Rashid, H., B. Flower, R. Poore, and T. Quinn (2007), A 25ka Indian Ocean monsoon variability record from the Andaman Sea, *Quat. Sci. Rev.*, *26*(19), 2586–2597.

Rein, B., A. Lückge, L. Reinhardt, F. Sirocko, A. Wolf, and W.-C. Dullo (2005), El Niño variability off Peru during the last 20,000 years, *Paleoceanography*, *20*, PA4003, doi:10.1029/2004PA001099.

Riedinger, M. A., M. Steinitz-Kannan, W. M. Last, and M. Brenner (2002), A 6100 14 c yr record of El Niño activity from the Galápagos Islands, *J. Paleolimnol.*, *27*(1), 1–7.

Roberts, W. H., D. S. Battisti, and A. W. Tudhope (2014), ENSO in the mid-Holocene according to CSM and HADCM3, *J. Clim.*, *27*(3), 1223–1242.

Rodbell, D. T., G. O. Seltzer, D. M. Anderson, M. B. Abbott, D. B. Enfield, and J. H. Newman (1999), A 15,000-year record of El Niño-driven alluviation in southwestern Ecuador, *Science*, *283*(5401), 516–520.

Rostek, F., G. Ruhland, F. Bassinot, P. Müller, L. Labeyrie, Y. Lancelot, and E. Bard (1993), Reconstructing sea surface temperature and salinity using δ^{18}O and alkenone records, *Nature*, *364*, 319–321.

Roxy, M. K., K. Ritika, P. Terray, and S. Masson (2014), The curious case of Indian Ocean warming, *J. Clim.*, *27*, 8501–8509.

Sandweiss, D. H., J. B. Richardson, E. J. Reitz, H. B. Rollins, and K. A. Maasch (1996), Geoarchaeological evidence from Peru for a 5000 years BP onset of El Niño, *Science*, *273*(5281), 1531–1533.

Sandweiss, D. H., K. A. Maasch, R. L. Burger, J. B. Richardson, H. B. Rollins, and A. Clement (2001), Variation in Holocene El Niño frequencies: Climate records and cultural consequences in ancient Peru, *Geology*, *29*(7), 603–606.

Sarkar, A., R. Ramesh, B. Somayajulu, R. Agnihotri, A. Jull, and G. Burr (2000), High resolution Holocene monsoon record from the Eastern Arabian Sea, *Earth Planet. Sci. Lett.*, *177*(3), 209–218.

Shukla, J., and D. Mooley (1987), Empirical prediction of the summer monsoon rainfall over India, *Mon. Weather Rev.*, *115*(3), 695–704.

Shukla, J., and D. A. Paolino (1983), The southern oscillation and long-range forecasting of the summer monsoon rainfall over India, *Mon. Weather Rev.*, *111*(9), 1830–1837.

Singh, G., R. D. Joshi, and A. Singh (1972), Stratigraphic and radiocarbon evidence for the age and development of three salt lake deposits in Rajasthan, India, *Quat. Res.*, *2*(4), 496–505.

Singh, G., S. Chopra, and A. Singh (1973), Pollen-rain from the vegetation of north-west India, *New Phytol.*, *72*(1), 191–206.

Singh, G., R. Joshi, S. Chopra, and A. Singh (1974), Late quaternary history of vegetation and climate of the Rajasthan Desert, India, *Philos. Trans. R. Soc. B*, *267*(889), 467–501.

Singh, G., R. Wasson, and D. Agrawal (1990), Vegetational and seasonal climatic changes since the last full glacial in the Thar Desert, Northwestern India, *Rev. Palaeobot. Palynol.*, *64*(1), 351–358.

Smith, T. M., R. W. Reynolds, T. C. Peterson, and J. Lawrimore (2008), Improvements to NOAA's historical merged land-ocean surface temperature analysis (1880-2006), *J. Clim.*, *21*(10), 2283–2296.

Sonzogni, C., E. Bard, F. Rostek, R. Lafont, A. Rosell-Mele, and G. Eglinton (1997), Core-top calibration of the alkenone index vs sea surface temperature in the Indian Ocean, *Deep Sea Res., Part II*, *44*(6), 1445–1460.

Sonzogni, C., E. Bard, and F. Rostek (1998), Tropical sea-surface temperatures during the last glacial period: A view based on alkenones in Indian Ocean sediments, *Quat. Sci. Rev.*, *17*(12), 1185–1201.

Staubwasser, M., F. Sirocko, P. Grootes, and M. Segl (2003), Climate change at the 4.2 ka BP termination of the Indus Valley civilization and Holocene south Asian monsoon variability, *Geophys. Res. Lett.*, *30*(8), 1425, doi:10.1029/2002GL016822.

Steinke, S., M. Kienast, J. Groeneveld, L.-C. Lin, M.-T. Chen, and R. Rendle-Bühring (2008), Proxy dependence of the temporal pattern of deglacial warming in the tropical South China Sea: Toward resolving seasonality, *Quat. Sci. Rev.*, *27*(7), 688–700.

Stott, L., C. Poulsen, S. Lund, and R. Thunell (2002), Super ENSO and global climate oscillations at millennial time scales, *Science*, *297*(5579), 222–226.

Stott, L., K. Cannariato, R. Thunell, G. H. Haug, A. Koutavas, and S. Lund (2004), Decline of surface temperature and salinity in the western tropical Pacific Ocean in the Holocene epoch, *Nature*, *431*(7004), 56–59.

Sukumar, R., R. Ramesh, R. Panti, and G. Rajagopalani (1993), A δ^{13}C record of late Quaternary climate change from tropical peats in Southern India, *Nature*, *364*(19), 703–706.

Swain, A., J. Kutzbach, and S. Hastenrath (1983), Estimates of Holocene precipitation for Rajasthan, India, based on pollen and lake-level data, *Quat. Res.*, *19*(1), 1–17.

Terray, P., and S. Dominiak (2005), Indian Ocean sea surface temperature and El Niño-Southern Oscillation: A new perspective, *J. Clim.*, *18*(9), 1351–1368.

Visser, K., R. Thunell, and L. Stott (2003), Magnitude and timing of temperature change in the Indo-Pacific warm pool during deglaciation, *Nature*, *421*(6919), 152–155.

Von Storch, H., and F. W. Zwiers (2001), *Statistical Analysis in Climate Research*, Cambridge Univ. Press, Cambridge, U. K.

Wasson, R., G. Smith, and D. Agrawal (1984), Late quaternary sediments, minerals, and inferred geochemical history of Didwana Lake, Thar Desert, India, *Palaeogeogr. Palaeoclimatol. Palaeoecol.*, *46*(4), 345–372.

Webster, P. (1987), The elementary monsoon, in *Monsoons*, edited by J. S. Fein and P. L. Stephens, pp. 3–32, John Wiley, New York.

Webster, P. J., V. O. Magana, T. Palmer, J. Shukla, R. Tomas, M. U. Yanai, and T. Yasunari (1998), Monsoons: Processes, predictability, and the prospects for prediction, *J. Geophys. Res.*, *103*(C7), 14,451–14,510.

Wu, G., Y. Liu, Q. Zhang, A. Duan, T. Wang, R. Wan, X. Liu, W. Li, Z. Wang, and X. Liang (2007), The influence of mechanical and thermal forcing by the Tibetan Plateau on Asian climate, *J. Hydrometeorol.*, *8*(4), 770–789.

Zhao, M., C.-Y. Huang, C.-C. Wang, and G. Wei (2006), A millennial-scale Uk'37 sea-surface temperature record from the South China Sea (8N) over the last 150 kyr: Monsoon and sea-level influence, *Palaeogeogr. Palaeoclimatol. Palaeoecol.*, *236*(1), 39–55.

Zhao, Y., P. Braconnot, O. Marti, S. Harrison, C. Hewitt, A. Kitoh, Z. Liu, U. Mikolajewicz, B. Otto-Bliesner, and S. Weber (2005), A multi-model analysis of the role of the ocean on the African and Indian monsoon during the mid-Holocene, *Clim. Dyn.*, *25*(7–8), 777–800.

Zheng, W., P. Braconnot, E. Guilyardi, U. Merkel, and Y. Yu (2008), ENSO at 6 ka and 21 ka from ocean-atmosphere coupled model simulations, *Clim. Dyn.*, *30*(7–8), 745–762.